Title
Keck AO survey of Io global volcanic activity between 2 and 5 mu m

Permalink
https://escholarship.org/uc/item/5346300m

Journal
Icarus, 176(1)

ISSN
0019-1035

Authors
Marchis, F
Le Mignant, D
Chaffee, F H
et al.

Publication Date
2005-07-01

Peer reviewed

Keck AO Survey of Io Global Volcanic Activity between 2 and 5μm

F. Marchis

Astronomy Department, University of California, Berkeley, California 94720-3411, U.S.A.

and

D. Le Mignant

W. M. Keck Observatory, 65-1120 Mamalahoa Hwy, Kamuela, Hawaii 96743, U.S.A.

and

F. H. Chaffee

W.M. Keck Observatory, 65-1120 Mamalahoa Hwy, Kamuela HI96743, U.S.A.

and

A.G. Davies

Jet Propulsion Laboratory, 4800 Oak Grove Drive, Pasadena, California 91109-8099, U.S.A.

and

S. H. Kwok

W. M. Keck Observatory, 65-1120 Mamalahoa Hwy, Kamuela, Hawaii 96743, U.S.A.

and

R. Prangé

Institut d'Astrophysique Spatiale, bat.121, Université Paris Sud, 91405
Orsay Cedex, France

and

I. de Pater

Astronomy Department, University of California, Berkeley, California
94720-3411, U.S.A.

and

P. Amico

W. M. Keck Observatory, 65-1120 Mamalahoa Hwy, Kamuela, Hawaii 96743,
U.S.A.

and

R. Campbell

W. M. Keck Observatory, 65-1120 Mamalahoa Hwy, Kamuela, Hawaii 96743,
U.S.A.

and

T. Fusco

ONERA, DOTA-E, BP 72, F-92322 Chatillon, France

and

R. W. Goodrich

W. M. Keck Observatory, 65-1120 Mamalahoa Hwy, Kamuela, Hawaii 96743,

U.S.A.

and

A. Conrad

W. M. Keck Observatory, 65-1120 Mamalahoa Hwy, Kamuela, Hawaii 96743,

U.S.A.

Received ————————; accepted ————————

Manuscript: 82 pages; 7 tables, 6 figures

Running title: Keck AO Survey of Io Global Volcanic Activity between 2 and 5 μm

Send correspondence to F. Marchis, University of California at Berkeley, Department of Astronomy, 601 Campbell Hall, Berkeley, CA 94720, USA

tel: +1 510 642 3958

e-mail: fmarchis@berkeley.edu

ABSTRACT

We present in this Keck AO paper the first global high angular resolution observations of Io in three broadband near-infrared filters: Kc (2.3 μm), Lp (3.8 μm) and Ms (4.7 μm). The Keck AO observations are composed of 13 data sets taken during short time intervals spanning 10 nights in December, 2001. The MISTRAL deconvolution process, which is specifically aimed for planetary images, was applied to each image. The spatial resolution achieved with those ground-based observations is 150, 240 and 300 km in the Kc, Lp and Ms band, respectively, making them similar in quality to most of the distant observations of the Galileo/NIMS instrument. Eleven images per filter were selected and stitched together after being deprojected to build a cylindrical map of the entire surface of the satellite. In Kc-band, surface albedo features, such as paterae (R > 60 km) are easily identifiable. The Babbar region is characterized by extremely low albedo at 2.2μm, and shows an absorption band at 0.9μm in Galileo/SSI data. These suggest that this region is covered by dark silicate deposits, possibly made of orthopyroxene. In the Lp-Ms (3-5 μm) bands, the thermal emission from active centers is easily identified. We detected 26 hot spots in both broadband filters over the entire

surface of the minor planet; two have never been seen active before, nine more are seen in the Ms band. We focused our study on the hot spots detected in both broadband filters. Using the measurements of their brightness, we derived the temperature and area covered by 100 brightness measurements. Loki displayed a relatively quiescent activity. Dazhbog, a new eruption detected by Galileo/NIMS in August 2001, is a major feature in our survey. We also point out the fading of Tvashtar volcanic activity after more than two years of energetic activity, and the presence of a hot, but small, active center at the location of Surt, possibly a remnant of its exceptional eruption detected in February 2001. Two new active centers, labeled F and V on our data, are detected.

Using the best temperature and the surface area derived from the L and M band intensities, we calculated the thermal output of each active center. The most energetic hot spots are Loki and Dazhbog, representing respectively 36% and 19% of the total output calculated from a temperature fit of all hot spots (20.6×10^{12} W). Based on the temperature derived from hot spots (~ 400 K), our measurement can unambigously identify the contribution to the heat flux from the silicate portion of the surface. Because the entire surface was observed, no extrapolation was required to calculate that flux. It is also important to note that we measured the brightness of the individual hot spots when they were located close to the Central Meridian. This minimizes the line-of-sight effect which does not follow strictly a classical cosine law. Finally, we argue that despite the widespread volcanic activity detected, Io was relatively quiescent in December 2001, with a minimum mean total output of 0.4–1.2 W m^{-2}. This output is at least a factor of two lower than those inferred from observations made at longer wavelengths and at different epochs.

1. INTRODUCTION

The discovery of volcanic activity on Io, the innermost Galilean satellite of Jupiter, by Voyager in March 1979 (Morabito *et al.* 1979), radically changed our vision of the satellites of the giant planets, as well as the evolution and interaction of bodies in our solar system in general. Near-infrared observations of Io during eclipse by Jupiter confirmed the hypothesis that a substantial amount of Io's energy is emitted in the 3 to 5 μm range by a number of small hot spots in the vicinities of the volcanoes (Sinton *et al.* 1980). The infrared spectrometer, IRIS, on board the two Voyager spacecrafts detected 10 volcanic centers Pearl and Sinton (1982) on a third of the satellite's surface. McEwen *et al.* (1992)'s subsequent analysis showed 7 more hot spots with typical 300 to 650 K temperature indicating a possible sulfur-based volcanic activity.

Thanks to the subsequent development of infrared (IR) detectors that allow monitoring of the total flux of Io from the ground (Veeder *et al.* 1994), our knowledge about the nature of this volcanism has expanded. Intense short-lived eruptions with a temperature greater than 1000 K were detected, indicating the presence of silicate volcanism on the satellite ((Johnson *et al.* 1988; Spencer *et al.* 1990; Blaney *et al.* 1995)).

A major goal of the Galileo mission, which arrived in the vicinity of Jupiter in June 1995, was to study the volcanism of Io. The spacecraft orbited Jupiter for seven years, providing a profusion of observations in the near-IR with its NIMS instrument (Lopes-Gautier *et al.* 1999; Lopes *et al.* 2001, 2004), in the visible with SSI (McEwen *et al.* 1998; Geissler *et al.* 1999) and in the mid-IR with the PPR photometer (Rathbun *et al.* 2004; Spencer *et al.* 2000). A eruption style has been determined at a number of

volcanoes on Io from a series of observations obtained throughout the Galileo mission. Early on it was recognised that different effusive styles had different spectra as seen by NIMS (Davies 2001). Attempts have been made to classify different eruption styles on Io, for example, "Pele-type" and "Prometheus-type" on the basis of plume type (McEwen and Soderblom 1983), and *Pillanean* (large pyroclastic deposits, short-lived, high volumetric eruption rate) and *Promethean* (long-lived, insulated flow fields with a sustained plume) (Keszthelyi *et al.* 2001). The term "Lokian" has been used to categorize patera volcanism (Lopes *et al.* 2004)), although two definitions are used, the first as "an eruption of a lava lake or lava flows within a patera which may or may not include plumes", and also as purely due to the presence of lava lakes in patera (see Radebaugh *et al.* 2001). To avoid this confusion, and to avoid naming a class after what appears to be a unique feature on Io (Loki) we use the term "Patera" volcanism to describe activity within patera, both flows and lava lakes. We note that a patera eruption becomes a Promethean eruption when the patera overflows (at Prometheus, for example, Davies 2003b). *Pelean* activity corresponds to vigorous resurfacing of a patera by the rapid replacement of the crust of a lava lake (seen at Pele), with sustained thermal emission at short infrared wavelengths. This is caused by continual exposure of high-temperature molten lava (Davies *et al.* 2001).

At the same time Galileo was providing high spatial resolution data of the surface of Io, the development of adaptive optics (AO) systems on ground-based telescopes gave astronomers the opportunity to monitor Io's volcanism from the ground with a resolution competitive with that provided by the spacecraft. Observations taken between 1996 and 2000 at 3.8 μm with the ESO 3.6-m AO-equipped telescope revealed the distribution and evolution of more than 20 low-temperature volcanic centers (Marchis *et al.* 2000, 2001).

More recently, observations at shorter wavelengths (1–2.5 μm) performed in February, 2001, with the Keck 10-m telescope indicate the presence of two high temperature (>800 K) eruptions coinciding with the Amirani and Tvashtar geographical areas. At the same epoch, on Io's other hemisphere, an extremely bright outburst located near the Surt volcano was observed at the beginning of its activity. Its temperature (>1400 K) and measured surface area lead to a calculated thermal flux close to the value estimated by Veeder *et al.* (1994) for the mean heat output of the entire satellite. This eruption remains the most energetic ever witnessed on the surface of Io (Marchis *et al.* 2002).

Io volcanism varies significantly with time. It remains unclear how its variation is distributed on the surface of the satellite; whether it is widespread or can be attributed to a few highly variable hot spots. To achieve a comprehensive study of the origin of Io's volcanism, its time evolution, and, more specifically, how tidal heating relates to this volcanism, one needs to monitor the volcanic activity on Io's surface and build a database of high spatial and temporal resolution. This is similar to what is being done to study terrestrial volcanism. There are now several ground-based 8 to 10 m telescopes and most of them can, or will soon be able to acquire high-angular resolution NIR images. With the end of the Galileo mission, the monitoring of Io lies in the hands of ground-based observers for the forseeable future.

We present in this paper the results of an extensive observing campaign of Io's surface using the Keck AO system and its near-IR camera NIRC2. Section 2 describes the data recorded in December 2001 and the data processing applied. These multi-wavelength data provided the opportunity to build high-angular resolution maps isolating albedo features and more than 26 active centers covering the entire surface of the satellite

(Sections 3 and 4). For the 26 hot spots detected at the longer wavelengths, we derived their location on the surface, temperature and area of their active centers (Section 5). In Section 6, we further focus our study on a sample of well-known, previously studied active hot spots and discuss the type and variability of their volcanic activity. Section 7 describes the relation between Io's calculated total thermal output and its volcanism.

The team responsible for this observing campaign has committed to publicly release all data presented in this paper.

2. OBSERVATIONS AND DATA PROCESSING

2.1. A Collaborative Effort

The W. M. Keck Observatory (Keck) with its twin 10-m hexagonal primary mirror telescopes is well-suited for very high angular resolution observations from the ground. The Keck AO system (Wizinowich *et al.* 2000) and its dedicated near-infrared NIRC2 camera, available on the Keck-II telescope, allow observations close to the diffraction limit of the telescope.

An observing program providing the full coverage of Io's surface at different wavelengths takes full advantage of the AO capabilities offered on Keck II. It also requires much flexibility in the scheduling of observing time. The Keck Observatory Director and scientific staff proposed this unique campaign to obtain high-angular resolution, multi-wavelength full coverage of Io's volcanic activity and elected to

collaborate on the project with the team of astronomers, mainly based at UC-Berkeley, that had already been allocated three nights with Keck AO/NIRC2. Their collaboration allowed scheduling of observations during a 10-night period, at appropriate times during the nights to cover Io's entire surface and to provide contingency in the case of non-photometric skies, poor seeing or technical problems. We were fortunate during that campaign, as none of the above problems occurred, providing a very uniform and high-quality data set on Io in three different broadband filters.

This campaign of monitoring Io's volcanic activity was scheduled between December 18 and 28, 2001 (UT), close to the 2002 opposition. Due to the proximity of the satellite (4.19 AU from Earth), the spatial resolution achievable on Io was nearly optimal. Using Keck AO, Io, subtending ~1.20 arcsec at the time of the observations, was exceptionally well resolved: the number of spatial resolution elements on its disc in the Kc, Lp and Ms band was 576, 225 and 144, respectively.

To achieve a regular and complete coverage of its surface, observations were scheduled at specific dates and times during this 10-day period corresponding to approximately 30° intervals in Central Meridian Longitude (CML).

Tables 1a and 1b contain the observational parameters in one narrow band filter called Kc (λ=2.2782 μm, $\Delta\lambda = 0.0296$ μm), and two broadband filters called Lp (3.776 μm, $\Delta\lambda = 0.700$ μm) and Ms (4.670 μm, $\Delta\lambda = 0.241$ μm) for each data set. Each observation within our December 2001 data set is labeled *DD*dec*HHMM* for which DD is the day of the observation and HHMM the approximate UT time. It should be noted

that 26dec1400 and 28dec0830 correspond to two data sets taken at similar CML ($\sim$220°).

2.2. Observations

Due to its brightness ($m_v \sim$5) and its small angular size ($\sim$1.20 arcsec), Io is ideally suited for use as the reference target for wavefront sensing. The Keck AO facility provides *nearly* diffraction-limited observations in the near-IR for most targets brighter than R=13.5 (van Dam *et al.* 2004). For bright targets such as Io, the AO system provides Strehl ratios as high as 60% at wavelengths longer than 2 μm. The data presented in this paper achieve an angular resolution within 10% of the diffraction limit of the Keck telescope for the observed wavelength.

For one instance in this data set, our wavefront sensing reference was Ganymede, which was more than 30 arcsec away from Io. This observation, `18dec0930`, was made near ingress of an eclipse of Io by Jupiter. The complete analysis for the Io-in-eclipse observations is presented in de Pater *et al.* (2004).

The NIRC2 camera (1024×1024 Aladdin-3 InSb array), specifically designed for high-angular resolution observations, provides imaging, long-slit spectroscopy and coronagraphy at three different plate scales. We used the narrow-field camera for our observations with a pixel scale of 9.94 mas ($\pm$5%)on the sky.

As many different observers were involved in the project, we used the NIRC2 scripting capabilities to make sure that all sets of observations would be recorded in

a consistent manner. For each CML, we tried to obtain: 1) images of Io in Kcont, Lp and Ms, 2) a measurement of the point spread function (a PSF calibrator star) that would be used later for image analysis and deconvolution, and 3) a photometric calibration. For PSF calibrators, we used stars located near the target and with the same visible magnitude (HIP30769, HIP33649, HIP33277, HIP30769, and HIP34861). In most cases, these stars served as flux standards as well. Additional photometric standards observed during the nights (HD22686, HD40335) are from the Elias catalogue (Elias *et al.* 1982). As evidenced by large variations in the Strehl ratio values in Tables 1a and 1b, we purposely de-activated the AO deformable mirror loop (high-order correction) for recording some of the photometric calibrations. The flux from the photometric calibrator is then spread over a wider area on NIRC2 in order to minimize the error from any deviant pixel.

During these 10 nights, the observer ran an observing script for each wavelength (Kcont, Lp or Ms), and the target (Io, PSF star or photometric standard). The target was recorded at 3 different positions on the 1024×1024 pixel images (in Kc band) or 512×512 pixel images in Lp and Ms bands. In particular, the dithering pattern and the number of frames per dither step were kept identical during the 10 nights for the three observed wavelengths. This allowed us to use the same data-reduction scripts for all data sets. Nonetheless, we preserved some flexibility in the NIRC2 scripting to optimize the observing efficiency by adjusting the integration time and the number of coadded frames at a given wavelength depending on the sky transparency, airmass and background emission (for Lp and Ms). This explains the slight variations of the total integration time for each observation in Tables 1a and 1b. Dedicated background frames for the three wavelengths were recorded in an area of the sky free of any bright star.

2.3. Data Processing and Calibrations

All data sets were processed in the same way using the *eclipse* software (Devillard 1997). Flat-field frames and bad pixel maps were generated using the uniformly illuminated sky frames. For each data set, the sky background was estimated by calculating the median average of the data cube composed of each frame. Flat-field and bad pixel corrections were applied. The mean value of the surrounding good pixel substituted for the value of each bad pixel. For the Io and PSF data, we discarded from the final shift-and-add process any frame with poor image quality introduced by, for instance, a minor technical problem or a sudden burst of bad seeing. The final image for each data set is the result of a shift-and-add of typically five frames. At the end of these data-processing steps, we obtained 14 images of Io taken in Lp, 13 images in Ms and 12 images in Kc. The 23dec1100 data were recorded in Lp only. The 22dec0730 data in Kc were taken without AO correction.

Tables 1a and 1b contain the list of PSFs and photometric stars observed during our program. The PSF star observations were reduced in a way similar to those of Io and were used to estimate the quality of the AO correction through measurement of the Strehl ratio (SR) and Full Width Half Maximum (FWHM). Each final basic-processed frame of Io is accompanied by 3 to 7 PSF star frames used for deconvolution purposes. The quality of the AO correction varied with the seeing conditions and the airmass at the time of the observations. The mean FWHM of the PSF star, i.e., the angular resolution of the data, is ∼50 mas in K-cont, ∼80 mas in Lp and ∼100 mas in Ms corresponding to a spatial resolution on the satellite near the central meridian of 150, 240 and 300 km, respectively. Individual measurements of the Strehl and the FWHM of PSFs are listed

in Tables 1a and 1b.

The zero-point measurements of each night at each wavelength were calculated using the observed photometric stars and cross-checked with the intensity of the PSF stars. Total fluxes and uncertainties were estimated by aperture photometry. The size of the optimal aperture varies with the quality of the AO correction, the observing wavelength and the signal-to-noise ratio in the image. The zero-point values obtained are consistent with those listed in the NIRC2 instrument technical Web page [1]. They are also extremely stable throughout the entire set of data, attesting to excellent photometric conditions during the observing nights: $Z_{Kc} = 21.5\pm0.1$, $Z_{Lp} = 23.5\pm0.1$, $Z_{Ms} = 21.4\pm0.2$. Zero-point values obtained on the same night (for instance on the 28decHHMM set) can be used to derive the accuracy of the absolute photometric measurements: 15% in Kc, 15% in Lp, and 24% in Ms.

2.4. Deconvolution

As discussed in the previous section, the angular resolution achieved on these December 2001 data sets is very uniform and excellent in most cases; measurements of the PSF stars show angular resolution values within 10% of the diffraction limit for the Keck telescope. The Strehl ratio, a common measurement of the quality provided on high angular data, is always >20%, and up to 75% in the Lp images, indicating good and stable correction. With such high signal-to-noise ratio, combined with

_____

[1]W. M. Keck Observatory, NIRC2 on-line Documentation, "NIRC2 sensitivity", http://www2.keck.hawaii.edu/inst/nirc2/sensitivity.html

excellent angular resolution, one can expect a significant improvement in the sharpness and sensitivity of the images after applying an *a posteriori* inversion process such as a deconvolution algorithm. We used MISTRAL (Myopic Iterative STep-preserving Restoration ALgorithm), a deconvolution algorithm developed by ONERA (Office National d'Études et de Recherches Aérospatiales), especially aimed at AO observations of planetary objects (Mugnier *et al.* 2004). MISTRAL uses a stochastic approach to find the best image reconstruction, using information about the object and the PSF. It requires several star images to evaluate variations in the PSF. The main improvement of this technique over more classical methods is that it avoids both noise amplification and creation of sharp-edged artifacts or "ringing effects" and it better restores the initial photometry. This algorithm has been extensively used on simulated and real AO observations (Conan *et al.* 2000; Marchis *et al.* 2001).

MISTRAL is not a straightforward deconvolution method. For each data set, we must provide a clean shift-added image and several frames of a PSF star. The algorithm balances the maximum-likelihood criterion with two regularization parameters, called *priors*. The first is called L1-L2 and permits the restoration of sharp edge in the image. The second is the myopic criterion which considers the variability of the PSF. The user weights each prior to achieve a good deconvolution. MISTRAL is an iterative method that requires a high number of iterations. An "under-regularized" image (for which the weights of the regularization parameters are too low) displays obvious pixelated artifacts as obtained with a classical Lucy-Richardson algorithm at high number of iterations (>1000). An "over-regularized image" keeps its blurry aspect and shows little improvement over the initial image. In this case, the values of the regularization parameters are too important, and the inversion process remains limited. Despite

its complexity, MISTRAL has provided excellent results for various planetary images recorded at different telescopes (Marchis *et al.* 2001, 2002; Hestroffer *et al.* 2002). We have intensively tested the method on real and artificial images. The resulting image contains considerably fewer artifacts than a classical Lucy-Richardson deconvolved image. The photometry is also conserved within an accuracy of 5–10% depending on the angular size and intensity of the structure.

The best deconvolved images for each data set are displayed in Figs 1a, 1b and 1c. The sharpness improvement is significant, and comparisons between images at roughly the same CML (26dec1400 and 28dec0830) clearly support the reality of structures observed on Io's surface (see discussion in Section 4).

Rather than discussing details of the deconvolution process, we discuss the possible problems of image artifact and photometry in Section 3.1 for the Kc images and Section 4 for the Lp and Ms images.

2.5. Public Release of the Data

The project team wishes to publicly release the data presented in this paper. The W. M. Keck Observatory hosts a Web site[2] that includes the processed data (cleaned images and deconvolved images), the map for Io at the three wavelengths as well as the data presented in the tables. The Web site also features a Java applet that allows the user to display interactively any location of Io's surface in one of the three wavelengths, compared to Galileo spacecraft's data. When the pointer passes over a hot spot, the tool

---

[2]W. M. Keck Observatory, http://www2.keck.hawaii.edu/science/io/

displays the name and the coordinates for the hot spot, as well as a subimage of the hot spot as observed by the Galileo spacecraft.

We also created a movie available in different video formats that shows Jupiter's volcanically active moon rotating. These materials have been presented elsewhere (Le Mignant *et al.* 2003).

3. ANALYSIS OF Kc-BAND IMAGES

Multi-wavelength imaging is of particular interest to allow the study of regions where the reflected solar flux dominates (Kc band) and those for which the thermal emissions from the volcanically active regions contribute significantly to the observed flux (mainly in Lp and Ms).

3.1. Albedo feature on the Kc-band images

In the Kc band (2.28 μm), the sunlight reflected by the surface of Io predominates over the thermal emission from the hot spots. For instance, on the 22dec1430 Kc image displayed in Fig. 1b, the bright feature close to the central meridian near the equator corresponds to the Bosphorus Regio, which is a large and well-known bright area in optical light supposedly covered with an SO_2 frost field (Douté *et al.* 2001). Its brightness is 0.20±0.01 GW/sr/μm, and it is the highest albedo area in Kc in our entire data set. For comparison, the mean brightness of the center of the disk is 0.13±0.03 GW/sr/μm. This hemisphere is also strewn with numerous circular dark areas which are identified as paterae, a possible source of volcanic eruptions. Twenty of them are clearly identified on the 22dec1430 Kc image. Their angular size is $\sim$70 mas, very close

to the limit of diffraction of the telescope. In comparison with the structures surrounding them, the brightness of the most centered ones is reduced by 0.04 GW/sr/μm. The nature of this dark material is still unclear, but it is generally interpreted as a floor covered with cold mafic or ultramafic magma (Radebaugh *et al.* 2001). Figure 2a shows a slightly bent vertical cut extracted on one of the images displayed in Fig. 1b along two paterae and the Bosphorus Regio. It must be emphasized that the hemisphere centered on CML$\sim$260° is characterized by a near absence of paterae, other than such major ones as Daedalus, Loki, Babbar, Pele, Isum, and a few minor ones (Reiden, Amaterasu, etc). This peculiarity (already reported in Radebaugh *et al.* (2001)) between the nearly Jupiter-facing and the anti-Jovian originate from an intrinsically different volcanic activity or by a different resurfacing rate due to the presence of active plumes.

Other Kc images also display gigantic dark regions believed to be dark pyroclastic deposits previously observed by Galileo/SSI (Geissler *et al.* 1999). The most obvious are those located around (43 S, 285 W), (20 S, 257 W), and (28 N, 209 W) corresponding respectively to the Babbar, Pele and Isum geographic features. Pele and Isum dark fields seem to be similar with a 70–80% contrast (in comparison with their surrounding area) and a radius $\sim$ 200 km. A bright peak, positioned at their center is clearly visible. Because of its profile, we infer that it is produced by an unresolved source, possibly an active hot spot (see section 6.5). The nature of Svarog dark area is more puzzling. With a size of $\sim$ 200km as well, its contrast is lower than 55%, indicating a different composition with darker material. Comparing the flux in the Kc (λ=2.2706 μm & $\Delta\lambda$= 0.0296 μm) band filter with several known reflectance spectra of solid surfaces, it is possible that the material in this large field corresponds to a dark silicate deposit. In fact, analysis of SSI data, also showed an absorption at 0.9 μm which suggested the presence

of orthopyroxene (Geissler *et al.* 1999). Our observation supports this interpretation, but further spectroscopic analysis is necessary to confirm the presence of this mineral. Babbar's deposit is larger than Pele's and fresher than Isum's, thus possibly explaining its larger spectral contrast. For comparison, apart from Babbar, a dark area with a contrast of only 60% can be observed into Zal Patera.

We selected 10 of the 13 data sets, discarding 1) that taken before the eclipse (18dec0930, see de Pater *et al.* (2004)), 2) that without the AO correction (22dec0730), and 3) the 28dec0830 set which was of lower quality than 24dec1400 taken at the same CML. The 28dec0830 Kc band image illustrates some of the artifacts arising from the application of sophisticated deconvolution algorithms to AO images, and provides eloquent warning in their interpretation: An abnormal ringing structure can be seen around the limb of the satellite with an intensity increase of 20%. This artifact is produced by the Gibbs effect which is a direct numerical effect introduced by any Fourier-based deconvolution method. Previous simulations (Hestroffer *et al.* 2002) show that the amplitude of the Gibbs effect seen in the images may be mitigated in the MISTRAL deconvolution algorithm by one of the regularization parameters called L1-L2. This parameter, when well-adjusted by the user, would have the effect of significantly reducing the intensity of the ring structure around the limb. Vice-versa, an inappropriate value for L1-L2 would worsen the artifact by increasing its intensity. The impact of this artifact has a low impact on the work presented in this paper, since we limited the analysis to the region close to the central meridian.

For each image, after visually fitting the limb, we deprojected it onto a cylindrical map. We built a 360-degree cylindrical map (Fig. 3) extracting a central strip for each data set and allowing for 10 pixels of overlap with the adjacent stripes. No photometric

corrections were applied to this map. The variation in flux of reflected sunlight is minimized, since the average width of the strip is 45 degrees. This map reveals the main albedo features on the surface of Io as observed in Dec. 2001. At larger resolution, it is quite comparable to the ones based on Voyager and Galileo/SSI observations.(McEwen *et al.* 1998).

4. ANALYSIS FROM THE LP AND MS OBSERVATIONS

The images in Lp and Ms are radically different from those in Kc. The thermal emission of the active volcanoes dominates over the reflected solar flux. Unresolved point sources seen on the surface of Io are called "hot spots", pointing out a high temperature location on Io (>120 K). (Sinton *et al.* 1980).

The Lp images still display large scale albedo features on the surface of the satellite, such as Babbar, Isum, and the dark high-latitude regions (see Fig. 3). The mean flux close to the sub-solar point is 0.3 GW/sr/μm. The integrated flux of the Ms data is dominated by the sunlit component (average intensity on the surface is 0.01 GW/sr/μm). Nevertheless, a significant portion of the Ms flux is produced by unresolved hot spots on the surface of the satellite. It is also possible that several hot and extended areas located on the surface contribute significantly to the Ms output.

After deconvolution several hot spots detected on the images appear to be surrounded by a bright ring, similar to the Airy ring around the PSF stars. Such features are particularly visible on the 20dec0930 and 28dec1400 images, which contain a hot spot close to the center of the disk. Fig. 2b is a cut along three hot spots visible in the 28dec1400 image. The ring artifacts are more intense in the Lp than in the Ms data.

Our experience in the deconvolution process with MISTRAL taught us that this ring is produced by a combination of the Gibbs effect and the variability of the PSF. Ms images are characterized by a high noise introduced by the background, but a very good AO correction. Kc band data have by contrast a low noise, and a highly variable PSF. Lp images are the most difficult to deconvolve because of the high level of their noise and the variability of the AO correction. Despite several attempts, we did not manage to obtain a deconvolved image without this artifact. A careful analysis of the images indicates that it appears only around very bright hot spots, for which the peak intensity is >0.05 GW/sr/μm. Such hot spots are easily detectable without deconvolution, and their photometry can be performed on non-deconvolved images as well. Comparison between the two photometric measurements shows that the ring artifact introduces a < 4% additional uncertainty in the photometric measurements.

The effectiveness and reliability of our deconvolution process is confirmed analyzing and comparing the 26dec1400 and 28dec0830 images (see Figs. 1b and 1c). These data were taken on two separate nights, but the same hemisphere of Io was observed. It is particularly interesting to compare them because the seeing conditions and airmass were significantly different, resulting in a variable image quality. However, despite these differences, after deconvolution, both images display the same albedo features (the Isum dark area, for instance) and the same hot spot distributions. We conclude that, when carefully applied, the MISTRAL deconvolution process is effective and the creation of artifacts is limited.

Using the technique described in Section 3.1, we built a cylindrical map based on the individual central strips of 11 deprojected cylindrical maps in Lp and Ms. The final Lp and Ms maps, displayed in Fig. 3, give a general view of the entire data set. In

Lp, albedo features are still visible, and unresolved thermal emission corresponding to active volcanic regions peppers the surface of the satellite. The Ms cylindrical map is characterized by a lower spatial resolution (300 km) due to the larger wavelength of observations. Nevertheless, because the contrast between the hot spot thermal emission and the sunlit flux is higher, plentiful bright eruptive centers are detected.

5. HOT SPOTS ON IO

Bright unresolved features, the so-called hot spots, detected on the disk of Io in Lp and Ms data correspond to active volcanic regions. To identify them on the surface of the satellite, we ran a kappa-sigma peak detection algorithm, using the eclipse software (Devillard 1997), on the Lp map looking for flux peaks 1.5 σ above the median pixel value and an FWHM on the map greater than 3 pixels. By this method, 34 peaks were detected. After removing those which are located on a ring artifact (around Pele and Janus), in the Bosphorus Regio, we identified 26 hot spots on the Lp map. We labeled these hot spots alphabetically (see map B on Fig. 3).

On the Ms map, we ran a similar detection process. The detection is relatively straightforward at this wavelength because of the higher contrast between the thermal emission of the hot spots and the sunlit flux. Additionally, the Ms band is characterized by fewer albedo features and fewer ringing artifacts (see previous section). In total, approximately 35 hot spots were detected and can be interpreted as hot spots on the surface map. For each hot spot identified in the Lp image, we could find its equivalent in the Ms map confirming its thermal emission origin. The hot spots that were detected

on the Ms map but not on the Lp map are either located in a bright albedo region in Lp, an artifact feature, and/or have a temperature too low to be detected in Lp. Their contribution to the thermal output calculated in Section 7 will be discussed.

5.1. Active Hot Spots: Position, Identification

Coordinates of the 26 hot spots detected in both Lp and Ms were estimated on the cylindrical Lp map by fitting the hot spots profile with a Gaussian. In addition to the uncertainties introduced by the fit, we added in quadrature an uncertainty of ~1/4 pixel on the fit of Io's limb position for targets located at high latitude ($> 35°$), increasing the error by $\sim 3°$. We identified each hot spot by comparing the coordinates with the volcanic centers detected by the Galileo spacecraft. Table 3 indicates their location in the planetary system coordinates. Candidate volcanic centers are compared with Lopes *et al.* (2003) which contains a list of hot spots detected by SSI and NIMS from eight years of Galileo observations. Half of these detected volcanic sites are labeled as "persistent" by Lopes-Gautier *et al.* (1999), analyzing the first 10 orbits of Galileo spanning 2 years, and including Voyager hot spots. To complete this list of persistent volcanoes, we should also add the three volcanoes Sengen, Daedalus and Fuchi paterae, located on the Jupiter-facing hemisphere, which was poorly observed during the Galileo mission, but regularly detected at high angular resolution from the ground since 1998 (Marchis *et al.* 2000, 2001). Our present analysis shows that 60% of the volcanic centers reported here are persistent eruptions. Most of them have been seen active for at least five and one-half years.

The surface features corresponding to these volcanically active centers are displayed in Figs. 4a and 4b. We used the global mosaic map based on the highest resolution SSI images presented in McEwen *et al.* (1998) to investigate the possible source of the eruption. Most of the displayed positions contain a dark patera feature. Two volcanic centers were previously unknown: F (49 N, 281 W) and V (39 S, 93 W). V is located in a region containing a well-defined ∼25-km-diameter patera, probably the source of the eruption. Due to the limited spatial resolution in some of our images, it is not always possible to clearly identify the origin of eruption. F, Tupan (Q), and Thor (R) hot spots show more than one patera within the area defined by the uncertainty of the position. The origin of the eruption is therefore unclear and several possible candidates can be considered. The positions of Surt (A) and Pillan (K) do not correspond to any patera feature on the SSI map. In fact, visible images taken during the Voyager 2 flyby (July 1979) exhibit a dark patera at the location of Surt. The images displayed in Figs. 4a and 4b are based on Galileo data taken in February 1997. The source of the eruption was not visible at that time, probably because it had been hidden by deposits coming from the plume of an active nearby volcano (see Marchis *et al.* 2002). A significant surface change was also observed during the eruption of the Pillan patera detected in May 1997 (Williams *et al.* 2001). The dark spot was interpreted as an ultramafic pyroclastic and lava flow deposit.

To better localize the source of these volcanic centers and possibly constrain the nature of their volcanism (lava lake, large flow, pyrosclatic deposit, etc), the region defined by our observations should be compared with the most recent high-angular resolution SSI data.

5.2. Active Hot Spots: Photometry and Intensity

The 26 Lp and Ms band hot spots can be seen independently in several data sets. Comparing consecutive data sets taken with a similar CML, we detect only one appearance of a new hot spot during our 10-day monitoring interval (see Section 6). No other hot spot disappeared or had an obvious change of activity. The activity of 25 hot spots was consequently quite stable during the 2001 Christmas period.

On each Lp and Ms image, we identified the hot spots found on the cylindrical map and measured their brightness. Tables 4a, 4b, 4c, and 4d contain the intensities in Lp and Ms of individual indentified active centers for each data set. They are labeled as in Table 3 with a letter suffix added to identify the particular hot spot (A for Surt, B for Fuchi, etc). In total, we measured 100 intensities of hot spots at two wavelength. The photometric measurement was done manually by aperture photometry for each hot spot on each deconvolved image. Several measurements were performed on the same target, varying the size of the integrated disk and/or the ring for the background estimate to take into account any possible variation due to an albedo feature located near the hot spot. The average and standard deviation of these measurements were then transformed into an intensity in GW/sr/μm using the closest in time zero-point measurement. The FWHM for each hot spot was also calculated. This measurement provides a good estimate of the spatial resolution on the disk after deconvolution. The Lp frames have an angular resolution $\sim$60 mas, indicating that the deconvolution process provides images which are hyper-resolved, i.e. with an angular resolution slightly smaller than that of the PSF, as expected.

In the same table, we also add the calculated brightness of each hot spot after applying a classical geometrical correction, i.e., dividing the intensity by the cosine of the angular

distance between the hot spot and the sub-Earth-point.

A brief study of the intensities presented in Tabs. 4a, 4b, 4c, and 4d shows that they are not always consistent for the same identified hot spot. For instance, Loki, one of the brightest hot spots, has reported Lp intensities of 14.8±0.5 on 18dec0730D, 4.3±0.4 on 20dec0730D, 28.8±2.9 on 28dec1215D and 21.9±0.7 on 28dec1400D (in GW/st/μm). This difference between measurements could have several origins. In fact, for each measurement an additional uncertainty exists because of the error bar of the zero-point measurements estimated to 15% in Lp and 25% in Ms (see discussion in Section 2.3). Additionally, as shown by Marchis *et al.* (2001), a cosine-law center-to-limb flux correction is inaccurate at high angles (>60 degrees). For example, they showed that the center-to-limb value of Pele's flux decreases slightly faster than a cosine law. This difference could be produced by the topography of the thermal source (e.g., the presence of a cliff surrounding the volcano) or, as proposed by Radebaugh *et al.* (2004), by a thermal eruption through cracks in the lava crust or by lava fountains. Taking all these realistic scenarios into account, a flux measurement, such as 20dec0730D performed with a 72° viewing angle, could be underestimated by a factor of two or three. Finally, the observations were taken over an interval of several days. The radiance of a hot spot can vary by a factor of 100 in a few days as illustrated during the observation of the 2001 Surt outburst (Marchis *et al.* 2002) or by a factor 10 as measured for the Loki volcanic eruption between 1999 and 2000 (Howell *et al.* 2001).

To better quantify the real error in the brightness intensity, two images were taken with the same central meridian ($\sim$ 220°) on 26dec1400 and 28dec0830. Due to the

42.5 h period of revolution of Io around Jupiter, the time difference between these two observations corresponds to the shortest delay between two observations of the same hemisphere of the planet. Because they were taken at different UT times on separate nights, their airmass and atmospheric transmission are different, making them an ideal image pair with which to estimate the uncertainty of our data.

For these two images, the absolute integrated intensities over the disk of Io differ by 6% and 33% in Lp and Ms, respectively. The intensities of the hot spots reported in Table 4c vary by 20% in Lp and 36% in Ms. Assuming an absence of volcanic activity flux change for these hot spots (a reasonable assumption over such a short interval), the measured difference is consistent with the uncertainties introduced through the entire analysis process, including the absolute photometric measurement (15% in Lp, 25% in Ms), the deconvolution process (5–10%) and the aperture photometry measurement (up to 5%).

The total intensity of the hot spots, which is the total volcanic flux of an image, can be compared with the integrated intensity on the disk as a function of the CML (see last column in Table 2a and 2b). The ratio of total thermal flux of the hot spots to solar-reflected flux varies significantly within their relative photometric accuracy. In Lp it fluctuates from 1% to 4% and 5% to 20% in Ms, with the maximum at CML=250–270°. These relative intensities are quite low compared to previous observations by Marchis *et al.* (2001) at similar wavelength (3.8 μm) who measured a thermal fraction of at least 10% and up to 24% in 1999-2000. This difference could result from the extremely low global volcanic activity of Io in December 2001 in comparison with that in 1999–2000. For example, the intensity of Loki varied from 40 to 120 GW/sr/μm between 1999–2000

and the intensity of Pele was >30 GW/sr/μm. In December 2001, the brightest intensities of Loki and Pele are measured in the 28dec1215 data set. Loki is up to three times fainter with an Lp brightness of $\sim$30 GW/sr/μm, Pele's brightness reaches only $\sim$9 GW/sr/μm. Since the main contributors to the thermal flux of Io are quiescent in December 2001, the ratio of thermal flux to solar-reflected flux varies slightly.

To summarize, 100 photometric measurements of 26 identified hot spots were performed on the entire set of data in Lp and Ms. We identified several sources of photometric uncertainties introduced by the absolute photometric measurement linked to the conversion of number of counts into flux through: 1) Zero-point estimates (15-25%), 2) the deconvolution process (5–10%), and 3) the measurement technique (up to 5%). It is clear that the main error is introduced by the line of sight correction which can underestimate by 200%-400% the flux of a hot spot with a viewing angle larger than 70°. For accurate study of the hot spot fluxes, in the following section of this paper we will focus on hot spot brightness measurements which were taken close to the CML.

5.3.   Temperature and Emission Area of Volcanic Centers

We extracted the 70 measurements in Table 4a, 4b, 4c, and 4d with vertical angle lower than 40°, limiting also a possible juxtaposition with another nearby hot spot. The radiance in L and Ms of each was fit by a classical single-temperature black body law considering that the emissive region corresponds to one single volcanic center. The fitting process used a classical χ^2-minimization method, and the transmission profile of the filter was included in the calculation, assuming a standard transmissivity of the atmosphere (McLean *et al.* 1998). Uncertainties on the temperatures were estimated by

varying the intensities within their error bar. The surface area of the emissive region was deduced using the best temperature fit obtained. Best estimates for the temperatures and their emission area are indicated in the Tables 5a, 5b and 5c. The mean temperature of the active areas is 400±70 K, very close to the temperature of a blackbody peaking at 5 μm. The highest temperature is measured on Pele with a value of 743±225 K. Hephaestus is the lowest temperature active area (280±90 K) detected in our data set. However this temperature is nearly three times the temperature of the non-active surface (95 K) as measured by the PPR photometer in a non-active areas (Rathbun *et al.* 2004). It is difficult to interpret the nature of the erupted lava flow on Io through these observations since the wavelength range of observations limits the sensitivity for extremely high temperatures expected at the core of an eruption. A small area of a few km^2 at a temperature of 1700 K would not be detected by our observations. Each measurement is in fact the mean temperature of the active center composed of a hot core and surrounded by cooling lava flow. Since our measurement can be considered a lower limit of temperature, we can conclude that several temperature measurements on most of the active centers (Surt, Sengen, F (unnamed), Pele, Isum, Marduk, Zamama, Culann, Tupan, Thor, Janus, Masubi) definitely rule out a pure sulfur-based lava eruption. Their temperature is greater than 450 K (Pearl and Sinton 1982), the liquidus temperature of a liquid sulfur lava flow on Io. Our measured temperatures are more appropriate for a basaltic-type eruption, analagous to volcanism observed on Earth.

6. ACTIVITY OF WELL-KNOWN VOLCANIC CENTERS

With the Galileo spacecraft orbiting in the Jovian system and the development of IR technology, several hot spots have been studied and monitored regularly for more

than five years. In this section, we focus on some of the hot spots and compare their activity with previous measurements.

6.1. Loki

Loki Patera is the most energetic permanent hot spot on Io. Because of its brightness in the NIR (>3 μm) it can be monitored from the ground without AO systems. Rathbun et al. (2002), showed a quasi-cyclic activity with a period of 540 days over 14 years, from studying the 3.5 and 3.8 μm activity. They proposed that Loki Patera might be a massive lava lake, with the cyclic activity caused by the foundering of the crust on the lake. High-resolution NIMS data of Loki Patera obtained in 2001 showed a temperature and age distribution on the floor of much of the Patera consistent with resurfacing by this mechanism Davies (2003a) while suggesting that resurfacing by flow emplacement was also possible. Our observations indicate an Lp-brightness ∼15-25 GW/sr/μm, similar to the one calculated on eclipse data by de Pater *et al.* (2004). The Lp/Ms ratio from our data suggests an active area with a mean temperature of 320–340 K, leading to a 3.5 μm-brightness of 8–15 GW/sr/μm. Comparing this brightness with previous measurements such as the 1999–2000 eruption described in Howell *et al.* (2001) we can infer that the volcanic activity of Loki was low at the end of December 2001. This faint activity was predicted by the cyclic activity analysis of Rathbun *et al.* (2002). However, Rathbun *et al.* (2003) reports an ending of the periodic behavior of Loki in 2000-2001. It is unclear when exactly started this non-periodic state. Our 3.5 μm-brightness seems to fit better the predicted activity than the ∼25 GW/sr/μm reported by Rathbun *et al.* (2003) on Dec. 12, 2001, but a variation of activity by 10 GW/sr/μm on 10 days was already observed by the same group. It is additionally interesting to note that the

active center is located in the southwest corner of Loki Patera. High-resolution PPR images taken during I24 (Spencer *et al.* 2000), and the NIMS I32 Loki observation (Davies 2003a) indicate that this area is constantly active, and the starting point for the resurfacing of the Patera floor.

6.2. Pillanean Volcanoes

Volcanic outbursts or *Pillanean* eruptions share several key characteristics: a short lived intense episode with high-temperature (>1400 K), fissure-fed eruptions producing both extensive pyroclastic deposits, and rapidly emplaced lava flows with open channels or sheets (Keszthelyi *et al.* 2001).

Dazhbog

Dazhbog was seen active during I31 (Aug. 2001) by Galileo/PPR instrument (Rathbun *et al.* 2004). Optical Galileo/SSI images of the region where this unexpected, high latitude, and bright outburst was located, showed the presence of a new red plume deposit (McEwen 2002). Four months latter, our data indicates that its brightness in Lp and Ms is still relatively important, comparable for instance to the Loki eruption. The temperature of ∼340 K and the measured extended area of ∼5200 km^2 imply that the eruption is mainly composed of an extended cooling lava flow. Observations in eclipse reported by de Pater *et al.* (2004) confirm the presence of a low-temperature lava flow and indicate the presence of a modest high-temperature core of ∼460 K.

Surt

The Surt hot spot is an extremely sporadic volcano. Since 1979, it has exhibited two major eruptions observed from the ground. Surt's eruption in 1979 was reported by

Sinton (1980) from photometric measurements in the thermal infrared. More recently, Marchis *et al.* (2002) detected an exceptionally bright outburst with the Keck AO system in February 2001 between 1–2.5 μm. Assuming a basaltic composition for the erupting magma, they showed that the eruption was extremely active with a temperature between 1030–1475 K in an area of approximately 800 km^2. Ten months later, a remnant of this outburst can still be detected in the Lp and Ms bands with a temperature of only 460 K and a compact area of 70 km^2. de Pater *et al.* (2004) detected thermal emission in K-band during an eclipse and derived a core temperature of 780 K in a small area of 2 km^2. The volcano is still active, though it has cooled considerably.

Tvashtar

The Tvashtar hot spot was discovered on November 1999 from the ground by Howell *et al.* (2001) and observed by the Galileo spacecraft during its flyby I25. Thought to be a sporadic outburst, this eruption was seen regularly from the ground (Marchis *et al.* 2001) as well with NIMS-SSI on board Galileo with magma temperatures exceeding 1000 K and showing extreme activity (Keszthelyi *et al.* 2001). The last report of activity by Marchis *et al.* (2002) in Feb. 2001 indicates a T∼810 K in an extended area of 460 km^2 and was interpreted as an average of a cooling lava flow region (with T=400-500 K) and an active fire fountain (with T>1400 K). Our data taken 10 months later do not show any evidence of activity in this area. Fig. 1a (22dec1100) indicates the expected position of the Tvashtar hot spot. In K band a dark caldera is clearly visible. No thermal emission can be detected in L or M bands. The Tvashtar eruption is either under the limit of detection of our data or the eruption is finally over after two years of intense activity. Based on the measured intensity and considering a limit of detection of 3σ for a hot spot, we can estimate that an eruption would have been seen in the Tvashtar

caldera if its Kc, Lp, and Ms band brightnesses are were at least 1.77, 1.01, and 1.70 GW/sr/μm respectively. Note that these brightnesses are half the intensity of Isum reported in Table 6. They can be considered as the limits of detection for this work, since they were calculated for a region located close to the limb (where reflected sunlight is minimized) and inside a dark caldera. In term of temperatures, considering that the Tvashtar emissive area covers 460 km^2 (as reported for Tvashtar 2001 in Marchis *et al.* (2002)), the minimum color temperature of the magma should be 500 K, and 330 K to be detected in K and L-M band respectively.

6.3. Promethean Volcanoes

Promethean volcanic centers have a long-lived, compound flow fields fed by insulated lava tubes or sheets. The length of the flow can be hundreds of kilometers. Eruptions seem to be able to continue for at least 20 years (Keszthelyi *et al.* 2001).

Amirani

A bright eruption on Amirani was detected between 1.6–2.5 μm in February 2001 by Marchis *et al.* (2002). From a blackbody fit they derived a T$\sim$1000 K and an active area of $\sim$100 km^2. Amirani is listed in Lopes-Gautier *et al.* (1999) as a persistent hot spot. It was seen as active on the first 10 orbits of Galileo, during the Voyager flybys, and from the ground (Marchis *et al.* 2001). Located on the anti-Jovian hemisphere of Io, this hot spot has rarely been studied from the ground. High spatial resolution images provided by SSI/Galileo show this region is the largest active lava flow known in our solar system. Its 2001 bright eruption was interpreted as a lava breakout from insulated flows in the Amirani field. In December 2001, the activity decreased significantly (no

thermal emission can be seen in Kc images), and our measurements indicated a mean temperature for the Amirani active magma of 350–400 K in an area of 200–500 km^2. A temperature close to the mean temperature ($\sim$420 km) was extracted from the profile along the lava flow field of Lopes *et al.* (2001). Our December 2001 observations might correspond to the normal state of activity of Amirani.

6.4. New Active Volcanic Centers

Thor

The volcanic area labeled R in our analysis, located at 36.4±5.9N, 134.7±7.2W corresponds to Thor, a newly discovered hot spot detected during the I31 Galileo' flyby and re-observed during I32 (Lopes *et al.* 2004). Our multi-wavelength analysis shows a magma temperature between 420–475 K extended over 110–350 km^2, indicating a cooling lava flow.

Unnamed-F and Unnamed-V

Two unknown active centers, labeled F and V in our analysis, were detected during our monitoring. Tables 3, 5a and 5c list their coordinates, temperature of the magma and area of the active surface.

Although unnamed-F (49N, 281W) is not visible in the 18dec0730 (CML=335°) images, it is easily detected in the images taken on December 28, 2001 (with a CML$\sim$ 260°). Considering its brightness in L and M bands (respectively 2.3 and 3.3 GW/sr/μm) and assuming a cosine law variation of brightness, we show that its peak intensity would

only 3-σ above the background variation. It is therefore unclear whether or not this hot spot appeared during our 10-day survey. The measurement of its brightness is also uncertain because it is located near the Dazhbog hot spot, and is relatively faint. From the one-temperature fit based on these measurement, we derived $340 < T < 860$ K with an extremely limited emission area of 5–20 km^2. This high temperature over a small area confirms the youth of this active center which is less than 10 days old. Using the Radebaugh *et al.* (2001, 2004) database we attempted to identify the source of the eruption. One patera fits very well with this hot spot location. It is numbered pv55 at 285.3 W and 53.4 N, and is 32.9 km by 41.6 km. It displays a dark mottled floor.

Unnamed-V (93.5 W, 39.5 S) is a radically different new active center. It is detected in four data sets (20dec0930, 22dec0730, 22dec1100, 22dec1430). Its Lp and Ms brightness ratio indicates a temperature of ∼360 K with an active area of ∼1000 km^2, a typical signature for a cooling lava flow. We identified two paterae that match the location of this hot spot using the Radebaugh *et al.* (2001, 2004) data base. One is numbered "p206" at 90.5 W and 36.4 S, and is 43.1 km by 37.6 km (35.8 km effective diameter) but does not display dark material at least when C21 SSI-mosaic images were taken. The second that fits is numbered "p207" at 91.9 W and 37.3 S, and is 28.9 km by 27 km. It has a dark mottled floor, and its location better matches that of unanamed-V. We propose naming this feature "Kalle" in reference to the legendary witch living close to the summit of *Piton de La Fournaise* on Reunion island, another volcanic island located in the Indian Ocean.

6.5.   Volcanoes with observed high brightness temperatures

Pele (J) is one of the most interesting hot spots on Io, as it exhibits every characteristic of being an active, overturning lava lake (Davies *et al.* 2001). Pele shows a preponderance of thermal emission at short IR wavelengths in every appropriate NIMS and SSI observations (Radebaugh *et al.* 2004). Even with the vigorous nature of volcanic activity, Pele nevertheless exhibits a near-constant thermal emission. Pele (J) and Isum (L) are both detected in the Kc images, an indication of considerable short-wavelength thermal emission. It should also be noted that these two active centers are located into a large low albedo surface feature, increasing the detectivity limit in the data. In fact, their peak intensity is approximately 0.17 GW/sr/μm. Thus, if they were located in a bright region such as Bosphorus Regio (which has a brightness of 0.20 GW/sr/μm, see Fig. 2a), their detection would have been marginal. Because we measure the brightness of these eruptions in three different wavelengths, it is possible to perform a more precise analysis of their activity using a basaltic cooling lava flow model.

6.5.1.   Analysis with a cooling basaltic lava model

The brightnesses on the Kc images was measured using the same aperture photometry technique described in the Section 5.2. We selected the 28dec0830 data set images since these were taken under good seeing and photometric conditions and both hot spots are located close to the central meridian, minimizing any possible geometrical effect.

Table 6 summarizes the intensity values extracted from the data in the three filters. To take into account the uncertainties introduced by the aperture photometry

measurement, we considered the two minimal and maximal intensities for each measurement. We fitted these data with a silicate cooling model (Davies 1996), originally developed to interpret ground-based Ionian observations and subsequently used to interpret Galileo/NIMS spectra (Davies 1996; Davies *et al.* 2000). In short, the model generates a series of thermal-emission spectra, with the number of areas at different temperatures being a function of the period of exposure of the hot lava surface. As time progresses, larger and cooler areas are added as the distant areas of the flow cool, with movement of the integrated thermal-emission spectrum to longer wavelengths. The model fit to the observational data consists of a spectrum comprising many individual blackbodies, the summed area of the individual areas, and the age of the oldest exposed surface. Using the total area of the flow and the exposure time, an average rate of areal increase can be calculated. Total area, temperature distribution and areal coverage rate are all a function of emplacement style. For example, fire fountains have short exposure times and high thermal intensity at short wavelengths, with a high areal coverage rate (Marchis *et al.* 2002). The relationship between eruption style (effusive or explosive, high or low volume, lava flows or lava lakes) and model output are described in greater detail in (Davies 1996) and Davies et al. 2001.

Assuming a basaltic composition for the eruption magma, the model fit to the eruption data produces a range of areas and temperature from 10^{-6} km^2 at 1450±0.5 K to less than 2 km^2 at ∼500 K. The oldest surface magma with a temperature of 473 K is 37.2 h old in the case of Pele. The Isum fit indicates a temperature of 771 K for the oldest surface magma (0.415 h). The total active area for Pele is relatively circumscribed (between 22–51 km^2) and extremely confined for Isum (∼1 km^2). The total flux output of the Pele eruptions (∼230 GW) is similar to the output derived

from the one-temperature fit based on the Lp and Ms intensity, indicating that a large fraction of the energy is produced by magma at a temperature of 400–500 K. The magma detectable at 2.2 μm (with a temperature $\sim$800–900 K) represents only 8% of its total output. In the case of Isum, the fraction of high temperature flux is much higher (40%). The model fit shows that the temperatures observed are very high, which means that little cooling has taken place, with the oldest emitting surface being approximately 6 minutes old. We can speculate that it started a few days, before or on December 26, date of the first detection on the surface of the satellite.

6.5.2. Interpreting the model output.

The (Davies 1996) model outputs for Pele and Isum are shown in Fig. 5 and Table 5b. Also shown in Figure 6 are model fits to NIMS observations of Gish Bar, Prometheus, Malik and Monan from Davies *et al.* (2000), and the model fit to the massive Surt outburst of 2001 (Marchis *et al.* 2002) for comparison. It is instructive to examine the activity at Pele and Isum in light of these models. Pele is seen to have a relatively small total area and a relatively young age. The lowest temperatures seen range from 473 K to 562 K. Figure 6 shows that the thermal emission from Gish Bar, Prometheus, Malik and Monan is dominated by large, relatively cool areas at temperatures down to 350 K. Pele and Isum are dominated by increased thermal emission at higher temperatures. The Surt outburst consists of relatively large areas at high temperatures, consistent with a large fire-fountain episode (Marchis *et al.* 2002). Pele is particularly interesting as it exhibits the same style of activity previously observed by NIMS and SSI (Davies *et al.* 2001). The peak of thermal emission at short wavelengths, the size of the emitting area and especially the total detected thermal emission (214 to 257 GW) are

very similar to that seen by NIMS over broadly the same wavelength range from 1996 through 2001 Davies *et al.* (2001). The constancy of activity at Pele indicates that the style of activity (the continual disruption of the crust on the surface of a lava lake; see Davies *et al.* (2001); Radebaugh *et al.* (2004) is continuing. At Isum, an areally small but thermally very vigorous eruption is underway. As seen in Fig. 5, the eruption is observed already in a more thermally active state than Pele, with larger areal coverage rates and greater thermal intensity reflected in the young age of the surface (less than 30 minutes). Although less total energy is being emitted at Isum, compared to Pele and the other volcanoes (except Surt), it is being emitted from larger areas at high temperatures (> 850 K) than at these volcanoes. This provides a clue as to the nature of activity at Isum. The style of volcanic activity that would produce this observed thermal emission and temperature/area distribution might be a tightly areally-confined eruption, perhaps in a patera or caldera, where flows cannot spread out; here, rapid resurfacing yields lava surfaces with young ages. The high areal coverage rate might be indicative of low-viscosity magma, or turbulent emplacement. A second eruption style is that of fire fountaining, yielding constant areas at high temperatures. The distinctive spectral signature of spreading, cooling flows which would lead to a shift in peak of thermal emission as the flow surfaces increase in size and cool is not seen. This is another indication of an areally confined activity. Subsequent observations of this location would be worthwhile. Once again, this demonstrates the need for high-temporal resolution monitoring of volcanic activity on Io. Snapshots of volcanic activity do not necessarily reveal the nature of the emplacement mechanism, but the temporal evolution of thermal activity invariably does (e.g., Davies et al., 2001; Rathbun et al., 2002).

7. POWER OUTPUT

7.1. Power Output Of Individual Volcanoes

Using the best temperature (T_{best}) and the surface area (S) derived from the Lp and Ms intensities, we calculated the total thermal output (F) using $F = S \times \sigma T_{best}^4$ (Table 5). This calculation shows that the most energetic hot spot is Loki (7.27×10^{12} W), followed by Dazhbog (3.82×10^{12} W). It is interesting to note that Dazhbog's power output was also measured through PPR data (Rathbun *et al.* 2004) on August 5, 2001 (I31) and October 15, 2002 (I32) and estimated as 3.59×10^{12} W and 4.38×10^{12} W respectively. Despite our observations having been recorded at shorter wavelengths, we measure a similar thermal output for this eruption. This is related to the relative young age of the eruption whose thermal output is still dominated by recent and hot magma flow. However, it reassures the reader that despite the long chain of data processing applied on the data, the final photometric measurements are accurate.

Figure 6 summarizes the total output for each volcano. With the exception of Loki and Dazhbog, none of them has an output greater than 10^{12} W. For comparison, the eruptions of Amirani and Tvashtar in February 2001, were significantly more energetic with a total output between $5–10 \times 10^{12}$ W. The largest thermal output attributed to Surt's erupting center was detected in February 2001 with a total ouput of $\sim 7.8 \times 10^{13}$ W (Marchis *et al.* 2001). Observations of the Jupiter-facing hemisphere detected during eclipse during the same period of time also indicate a low thermal output for the active volcanoes (de Pater *et al.* 2004).

7.2. Total Output of Active Volcanism

The total outputs of the active volcanoes detected with these AO data and calculated here using the temperature and area derived from the Lp/Ms ratio and brightness (Table 5), correspond only to the hottest part of the volcanic activity. As shown in Section 5.3, the mean temperature estimated for all hot spots is 400±70 K, with a minimum temperature of 285 K and a maximum of 540 K. Using the basaltic cooling lava flow model presented in Section 6.5, we can estimate the age of these eruptions. A 400 K-temperature fit corresponds to lava ejected 6-7 days ago. The oldest lava field (seen at Fuchi hot spot with a fitted temperature of 285 K) is 150-200 days old.

Therefore, our measurements can unambiguously identify the silicate portion of the heat flux from the surface. Additionally, they are based on data covering the entire surface of the satellite, implying that no extrapolation was required to calculate it. Our global observations clearly show the inhomogeneity of the thermal output of individual hot spots (see Fig. 6). For instance two volcanic centers (Loki and Dazhbog) located in the same region of the satellite contribute 55% of its total output. A calculation of the total output based only on this observed hemisphere would have led to an overestimate of the total output by at least a factor of 4.

To better consider the uncertainties in the fit introduced by the photometric error, we calculated the total output using the minimum and maximum output of each hot spot. The calculated output of a hot spot varies because of differences in the fit introduced by uncertainties in the photometry and from the geometry of the observation as described in Section 5.2. This method appears to be the best way to obtain a good estimate of the total output considering all those instrumental and photometric uncertainties. The maximum total output (24.5 x10^{12} W) and minimum output (16.6 ×10^{12} W) lead to a

mean total output of 0.39–0.58 W m^{-2}.

This is an interesting result, since it is the first time the mean total output from Io's entire surface is derived at shorter wavelengths (2-5μm) considering the flux of resolved sources of active volcanism. Since this energy is attributed to active and young volcanism only, it can be considered as a lower limit to Io's total volcanic output.

Other measurements taken at longer wavelengths have implied luminosities up to five times higher (2.5 W m^{-2} for Veeder *et al.* (1994), 2.6 W m^{-2} for McEwen *et al.* (1992)). de Pater *et al.* (2004) also reports a low average total output of 0.2 W m^{-2} based upon the observations of the Jupiter-facing hemisphere in K, L and M bands in eclipse, implying that most of the faint active sources undetected on our sunlit images do not contribute significantly to the total output.

The contribution of hot spots detected only in the Ms band (with T <300 K) to the total thermal output cannot be estimated. Comparing carefully the Lp and Ms maps on Fig. 3, we can infer that 3 of them exhibit an extremely low thermal signature in Lp band. Considering as an upper limit for their brightnesses the limit of detection calculated in section 6, their contribution to the thermal output remains marginal (<0.15 W/m^2). For those which are seen only in Ms band without any emission in Lp band, their thermal flux, if they are real, cannot be calculated without the recording of longer wavelength data.

7.3. Refining Io Average Heat Flow

Considering the temperatures involved in the best fit of the active centers, it is clear that a large fraction of the active part of the Io silicate-based volcanism is detected

in these data. A quantitative estimate of the unobserved longer-wavelength flux is a difficult exercise because of the lack of simultaneous high angular resolution data taken in this wavelength range.

To estimate the amount of total output missed by our measurements, we compared the power outputs of several PPR hot spots detected by Galileo in I31 and I32 and reported in Rathbun *et al.* (2004). Our observations were taken 4 months after I31 and 10 months before I32. Table 1 shows the power outputs measured for 9 active centers which were detected in this data set and by Galileo/PPR. In comparison with I31 power output, our measurements for most of the volcanoes are underestimated, indicating that the contribution from the low-temperature component is undetected. The Pillan eruption output constitutes the worst case with an output 4 times smaller than the one based on PPR I31, but only twice as small if compared with PPR I32. It should be noted that the Pillan photometric measurements are also complicated by the close location of Pele whose activity is strong. A part of the Pillan flux may have been attributed to Pele during the measurements. We also reported in Tab. 1 the power output calculated through the basaltic lava cooling flow model for Isum and Pele. They are not closer to PPR data than our simple calculation mainly because in this case a large amount of energy is provided by a young active center whose activity should be extremely variable on a period of time shorter than a month. It is therefore difficult to compare their activity with Galileo PPR measurements taken several months before or after.
To conclude, the average ratio of I31 power output to our measurements is estimated to be $\sim$1.9. Intrinsic variations of power output due to changes in the activity of these 9 hot spots can be estimated comparing I31 and I32 PPR measurements. In average their total outputs are quite stable with a ratio of $\sim$1.1. Considering that our power output

calculation underestimates the real power output of the volcanoes, its impact on the mean total output is however limited. This comparison shows that in the nearest case it may be low by a factor of two, bringing the average heat flow produced by young and active volcanoes to between 0.4 and 1.2 W m^{-2}.

This measurement remains at least a factor of two lower than the mean total output published by Veeder *et al.* (1994), and more recently by Veeder *et al.* (2004). Io's surface temperature is complex and ground-based observations in the mid-IR ($>10\mu$m) (Veeder *et al.* 1994) indicate that a large part of the total thermal output comes from extended areas on the surface which are believed to be old cooling lava flow fields at temperatures below 200 K. Whether these large warm fields are indeed purely volcanic in origin is unclear. Lei-Kung Fluctus, for instance, shows a temperature of 130 K at night (Rathbun *et al.* 2004) over 20 years of observations, only 40 K above the average surface temperature. The authors attribute the energy at least in part to volcanism. However, no detailed calculations have been carried out regarding solar radiation balance for different types of 'rock' (e.g., high thermal inertia) or the magnetic field of Jupiter (by particle bombardment). Most published values for Io's heat flow are model dependent, and assume that the heat flux arises from cooling lava flows. One can also presume that purely sulfuric volcanism, as with hydrothermal volcanoes on Earth, may play a major role in transporting heat from the inside to the outside of Io (L. Keszthelyi, personal communication).

If our measurement of 0.4-1.2 W m^{-2} (1.7–5 $\times$ 10^{13} watts total) is considered as the true mean total output of Io, it solves several previously-unresolved problems: 1) coupled thermal-orbital evolution models developed by Hussmann and Spohn (2004)

which are based upon an orbital evolution of Io, Europa, and Ganymede into the Laplace resonance indicate a heat production rate of $\sim 2 \times 10^{13}$ W at the present time; 2) Lieske (1987) calculated a dissipated energy of $\sim 2 \times 10^{13}$ W from secular changes in the mean motion of Io; and 3) such a low heat flow value would be in agreement with a conductive lithosphere more than 10 km thick as shown by Hussmann and Spohn (2004). A thick lithosphere would be able to support Ionian mountains higher than 10 km as observed in Galileo data (Schenk *et al.* 2001).

It is worthy to note that since the volcanic activity of Io was quiescent in December 2001, as shown by the absence of bright outbursts and the relatively low activity of Loki, the total output derived here can be regarded as the minimum thermal output of Io volcanism. In the future, the study of variations in the thermal output over a large period of time may yield interesting information on the evolution of Io, Europa, and Ganymede into the Laplace resonance through tidal dissipation.

8.   CONCLUSION

We presented in this paper global high angular resolution Keck AO observations of Io in three broadband near-infrared filters: Kc (2.3 μm), Lp (3.8 μm) and Ms (4.7 μm). The entire set is composed of 13 series of images taken over a 10-day period in December 2001. The MISTRAL (Mugnier *et al.* 2004) deconvolution process specifically developed for planetary science images was applied to each image. The spatial resolution reached with these ground-based observations is 150 km in Kc, 240 km in Lp band and 300 km in Ms band, making them competitive with most of the Galileo/NIMS spacecraft observations. Eleven images per filter were selected and stitched together after being

deprojected to build a cylindrical map of the entire surface of the satellite (Fig. 3). We also publicly released the entire data set.

In the Kc, surface albedo features, such as paterae (R>60 km), are easily identifiable. The difference between the number of large paterae between the Jupiter-facing hemisphere and non-Jupiter-facing is confirmed by our data. This difference may be due to an intrinsically different type of volcanic activity or to a different resurfacing rate due to the presence of active plumes between both hemispheres of Io. The Kc map showed also that the Babbar region is characterized by an extremely low albedo. Considering that orthopyroxene is characterized by two absorption bands, one at 0.9 μm which was detected by Galileo/SSI in this region (Geissler *et al.* 1999), and another at 2.2 μm observed here, we suggest that Babbar Patera is covered by an orthopyroxene deposit "fresher" that Isum's and scattered over an area larger than for the Pele Patera.

In Lp–Ms (3-5 μm), the thermal emission from active centers is easily discerned. We detected 26 hot spots observed in both broadband filters over the entire surface of Io ; nine more are seen only in Ms. We focused our study on the hot spots detected in both filters. Using the 70 best brightness measurements, we derived the temperatures and areas covered by the flows. For the most well-known volcanic centers, we compared the type of their activity with the information provided by Galileo NIMS/SSI instruments. We show, for instance, that Loki has relatively quiescent activity as predicted by Rathbun *et al.* (2002). Dazhbog, a new eruption detected by Galileo/NIMS in August 2001 (Lopes *et al.* 2004), is a major eruption in our survey. We also noted the fading of the Tvashtar eruption after more than two years of activity, and the presence of a hot, but small, active center at the location of Surt, possibly a remnant of its exceptional

eruption detected in February 2001 (Marchis *et al.* 2002). We detect two new active centers, labeled F and V on our data. For both, we detected the most likely patera source of the eruption via comparison with Radebaugh *et al.* (2004)'s database.

Two hot spots, Isum and Pele, also exhibit a thermal signature in Kc. Combining the three broadband brightnesses, we derived the type of activity using a basaltic cooling lava flow model (Davies 1996). Pele exhibits the same style of activity previously observed by NIMS and SSI (Davies *et al.* 2001) indicating that the style of activity (the continual disruption of the crust on the surface of a lava lake; see Davies *et al.* (2001) and Radebaugh *et al.* (2004)) is continuing. At Isum, an areally small but thermally very vigorous eruption is under way, indicative of either i) a tightly areally-confined eruption, perhaps in a patera or caldera, where flows cannot spread out; or ii) a small fire fountaining eruption, yielding constant areas at high temperatures. Subsequent observations of this location could show if extensive flows form, or if the lava remains areally confined. This, once again, demonstrates the utility of high-temporal resolution monitoring of volcanic activity on Io.

Using the best temperature and the surface area derived from the Lp and Ms band intensities, we calculated the total thermal output for each measurement (Table 5). The most energetic hot spot is Loki ($7.27\mathrm{x}10^{12}$ W), followed by Dazhbog (3.82×10^{12} W), representing respectively 40% and 20% of the minimal value of average heat flow calculated from the 26 detected active centers. We have shown that the heat flow calculated here originates from silicate volcanism, and can be considered a lower limit to the thermal output of Io's volcanism. Considering Galileo/PPR measurements this

can be estimated to be between 0.4 and 1.2 W m^{-2}. This measurement is at least twice lower than the one derived by Veeder *et al.* (1994) based on a survey of Io at 10-20 μm because it does not include thermal emission from low-temperature extended areas on the surface. We briefly discussed the consequences for such small mean total output, which is attractive because it solves several important problems. It is compatible with the heat production rate predicted by Hussmann and Spohn (2004) based on an evolutionary model of Io, Europa, and Ganymede into the Laplace resonance. It is close to the dissipated energy calculated by Lieske (1987) from secular changes in the mean motion of Io.

Our knowledge about Io's volcanic activity is incomplete. It began with its discovery during the first Voyager flyby in 1979, preceded and followed by monitoring from the ground, and could have ended with the exceptional insights provided by the 10-yr long Galileo mission. These data clearly attest to the variability of this extraordinary volcanism. To really understand how Io evolved and how tidal heating and loss processes balance overall, we need to build a database of high spatial and temporal resolution over a large period of time, just as the one being used to study terrestrial volcanism. With the Keck AO global coverage of Io's volcanism presented here, we are starting to fill the gap between the Galileo mission and JIMO (Jupiter Icy Moons Orbiter), the next ambitious mission toward Jupiter scheduled to be launched after 2012.

Acknowledgments

REFERENCES

Blaney, D. L., T. V. Johnson, D. L. Matson, and G. J. Veeder 1995. Volcanic eruptions on Io: Heat flow, resurfacing, and lava composition. *Icarus* **113**, 220–225.

Conan, J.-M., T. Fusco, L. Mugnier, F. Marchis, C. Roddier, and F. Roddier 2000. Deconvolution of adaptive optics images: from theory to practice. In P. Wizinowich (Ed.), *Adaptive Optical Systems Technology*, Volume 4007, Bellingham, Washington, pp. 913–924. SPIE.

Davies, A. G. 1996. Io's Volcanism: Thermo-Physical Models of Silicate Lava Compared with Observations of Thermal Emission. *Icarus* **124**, 45–61.

Davies, A. G. 2001. Volcanism on Io: the view from Galileo. *Astronomy and Geophysics* **42**, 2.10–2.15.

Davies, A. G. 2003a. Temperature, age and crust thickness distributions of Loki Patera on Io from Galileo NIMS data: Implications for resurfacing mechanism. *Geophys. Res. Lett.* **30**, 2133–2136.

Davies, A. G. 2003b. The Pulse of the Volcano: Discovery of Episodic Activity at Prometheus on Io. In *Lunar and Planetary Institute Conference Abstracts*, pp. 1455–+.

Davies, A. G., L. P. Keszthelyi, D. A. Williams, C. B. Phillips, A. S. McEwen, R. M. C. Lopes, W. D. Smythe, L. W. Kamp, L. A. Soderblom, and R. W. Carlson 2001. Thermal signature, eruption style, and eruption evolution at Pele and Pillan on Io. *J. Geophys. Res.* **106**, 33079–33104.

Davies, A. G., R. Lopes-Gautier, W. D. Smythe, and R. W. Carlson 2000. Silicate Cooling Model Fits to Galileo NIMS Data of Volcanism on Io. *Icarus* **148**, 211–225.

de Pater, I., F. Marchis, B. A. Macintosh, H. G. Roe, D. Le Mignant, J. R. Graham, and A. G. Davies 2004. Keck AO observations of Io in and out of eclipse. *Icarus* **169**, 250–263.

Devillard, N. 1997. The eclipse software. *The Messenger* **87**, 119–123.

Douté, S., B. Schmitt, R. Lopes-Gautier, R. Carlson, L. Soderblom, J. Shirley, and T. The Galileo NIMS Team 2001. Mapping SO_2 Frost on Io by the Modeling of NIMS Hyperspectral Images. *Icarus* **149**, 107–132.

Elias, J. H., J. A. Frogel, K. Matthews, and G. Neugebauer 1982. Infrared standard stars. *AJ* **87**, 1029–1034.

Geissler, P. E., A. S. McEwen, L. Keszthelyi, R. Lopes-Gautier, J. Granahan, and D. P. Simonelli 1999. Global Color Variations on Io. *Icarus* **140**, 265–282.

Hestroffer, D., F. Marchis, T. Fusco, and J. Berthier 2002. Adaptive optics observations of asteroid (216) Kleopatra. *A&A* **394**, 339–343.

Howell, R. R., J. R. Spencer, J. D. Goguen, F. Marchis, R. Prangé, T. Fusco, D. L. Blaney, G. J. Veeder, J. A. Rathbun, G. S. Orton, A. J. Grocholski, J. A. Stansberry, G. S. Kanner, and E. K. Hege 2001. Ground-based observations of volcanism on Io in 1999 and early 2000. *J. Geophys. Res.* **106**, 33129–33140.

Hussmann, H., and T. Spohn 2004. Thermal-orbital evolution of Io and Europa. *Icarus* **171**, 391–410.

Johnson, T. V., G. J. Veeder, D. L. Matson, R. H. Brown, and R. M. Nelson 1988. Io - Evidence for silicate volcanism in 1986. *Science* **242**, 1280–1283.

Keszthelyi, L., A. S. McEwen, C. B. Phillips, M. Milazzo, P. Geissler, E. P. Turtle, J. Radebaugh, D. A. Williams, D. P. Simonelli, H. H. Breneman, K. P. Klaasen, G. Levanas, T. Denk, and Galileo SSI Team 2001. Imaging of volcanic activity on Jupiter's moon Io by Galileo during the Galileo Europa Mission and the Galileo Millennium Mission. *J. Geophys. Res. 106*(E12), 33025–33052.

Le Mignant, D., F. Marchis, S. H. Kwok, P. Amico, R. D. Campbell, F. H. Chaffee, A. Conrad, A. R. Contos, R. Goodrich, G. M. Hill, D. Sprayberry, P. J. Stomski, P. L. Wizinowich, and I. de Pater 2003. Io, the movie. In P. Guhathakurta (Ed.), *Discoveries and Research Prospects from 6- to 10-Meter-Class Telescopes II.*, Volume 4834, pp. 319–328. SPIE proceeding.

Lieske, J. H. 1987. Galilean satellite evolution - Observational evidence for secular changes in mean motions. *A&A* **176**, 146–158.

Lopes, R. M. C., L. W. Kamp, S. Douté, W. D. Smythe, R. W. Carlson, A. S. McEwen, P. E. Geissler, S. W. Kieffer, F. E. Leader, A. G. Davies, E. Barbinis, R. Mehlman, M. Segura, J. Shirley, and L. A. Soderblom 2001. Io in the near infrared: Near-Infrared Mapping Spectrometer (NIMS) results from the Galileo flybys in 1999 and 2000. *J. Geophys. Res.* **106**, 33053–33078.

Lopes, R. M. C., L. W. Kamp, W. D. Smythe, R. Howell, P. Mouginis-Mark, J. S. Kargel, J. Radebaugh, E. P. Turtle, J. Perry, D. A. Williams, R. W. Carlson, S. Doute, and Galileo NIMS Team 2003. Lava Lakes on Io? *AAS/Division for Planetary Sciences Meeting* **35**, –+.

Lopes, R. M. C., L. W. Kamp, W. D. Smythe, P. Mouginis-Mark, J. Kargel, J. Radebaugh, E. P. Turtle, J. Perry, D. A. Williams, R. W. Carlson, and S. Douté 2004. Lava lakes on Io: observations of Io's volcanic activity from Galileo NIMS during the 2001 fly-bys. *Icarus* **169**, 140–174.

Lopes-Gautier, R., A. S. McEwen, W. B. Smythe, P. E. Geissler, L. Kamp, A. G. Davies, J. R. Spencer, L. Keszthelyi, R. Carlson, F. E. Leader, R. Mehlman, L. Soderblom, The Galileo Nims, and SSI Teams 1999. "active volcanism on io: Global distribution and variations in activity". *Icarus* **140**, 243–264.

Marchis, F., I. de Pater, A. G. Davies, H. G. Roe, T. Fusco, D. Le Mignant, P. Descamps, B. A. Macintosh, and R. Prangé 2002. High-Resolution Keck Adaptive Optics Imaging of Violent Volcanic Activity on Io. *Icarus* **160**, 124–131.

Marchis, F., I. de Pater, H. G. Roe, T. Fusco, D. Le Mignant, B. A. Macintosh, and S. Acton 2001. Report on the io volcanic activity observed from the ground with the adonis eso and keck ao systems. In *Jupiter Meeting*, Volume Colorado. Boulder.

Marchis, F., R. . Prangé, and J. Christou 2000. Adaptive Optics Mapping of Io's Volcanism in the Thermal IR (3.8 μm). *Icarus* **148**, 384–396.

Marchis, F., R. . Prangé, and T. Fusco 2001. A survey of Io's vocanism by adaptive optics observations in the 3.8-μm thermal band (1996-1999). *J. Geophys. Res.* **106**, 33141–33160.

McEwen, A. S. 2002. Volcanic Plumes on Io: Old Friends and Recent Surprises. *AGU Spring Meeting Abstracts*, A2+.

McEwen, A. S., N. R. Isbell, and J. C. Pearl 1992. Io Thermophysics: New Models with Voyager I Thermal IR Spectra. In *Lunar and Planetary Institute Conference Abstracts*, pp. 881–+.

McEwen, A. S., L. Keszthelyi, P. Geissler, D. P. Simonelli, M. H. Carr, T. V. Johnson, K. P. Klaasen, H. H. Breneman, T. J. Jones, J. M. Kaufman, K. P. Magee, D. A. Senske, M. J. S. Belton, and G. Schubert 1998. Active Volcanism on Io as Seen by Galileo SSI. *Icarus* **135**, 181–219.

McEwen, A. S., and L. A. Soderblom 1983. Two classes of volcanic plumes on Io. *Icarus* **55**, 191–217.

McLean, I. S., E. E. Becklin, O. Bendiksen, G. Brims, J. Canfield, D. F. Figer, J. R. Graham, J. Hare, F. Lacayanga, J. E. Larkin, S. B. Larson, N. Levenson, N. Magnone, H. Teplitz, and W. Wong 1998. Design and development of NIRSPEC: a near-infrared echelle spectrograph for the Keck II telescope. In A. M. Fowler (Ed.), *Infrared Astronomical Instrumentation*,, Volume 3354, pp. 566–578. SPIE proceeding.

Morabito, L. A., S. P. Synnott, P. N. Kupferman, and S. A. Collins 1979. Discovery of currently active extraterrestrial volcanism. *Science* **204**, 972–972.

Mugnier, L., T. Fusco, and L. Conan 2004. MISTRAL : a Myopic Edge-Preserving Image Restoration Method. Application to Astronomical Adaptive Optics Corrected Long-Exposure Images. *JOSA* **21**, 1841–1854.

Pearl, J. C., and W. M. Sinton 1982. Hot spots of Io. In D. Morrison (Ed.), *Satellites of Jupiter*, Tucson, Arizona, pp. 724–755. University of Arizona Press.

Radebaugh, J., W. L. Jaeger, L. P. Keszthelyi, E. P. Turtle, M. P. Milazzo, J. Perry, A. S. McEwen, R. Lopes, A. G. Davies, and P. Geissler 2004. Relationships Between Paterae, Mountains, and Hotspots on Io from a Global Database. In *Lunar and Planetary Institute Conference Abstracts*, pp. 2067–+.

Radebaugh, J., L. P. Keszthelyi, A. S. McEwen, E. P. Turtle, W. Jaeger, and M. Milazzo 2001. Paterae on Io: A new type of volcanic caldera? *J. Geophys. Res.* **106**, 33005–33020.

Radebaugh, J., A. S. McEwen, M. P. Milazzo, L. P. Keszthelyi, A. G. Davies, E. P. Turtle, and D. D. Dawson 2004. Observations and temperatures of Io's Pele Patera from Cassini and Galileo spacecraft images. *Icarus* **169**, 65–79.

Rathbun, J. A., S. T. Johnson, and J. R. Spencer 2003. Loki, Io: An Update on Activity from Groundbased Data. In *Lunar and Planetary Institute Conference Abstracts*, pp. 1375–+.

Rathbun, J. A., J. R. Spencer, A. G. Davies, R. R. Howell, and L. Wilson 2002. Loki, Io: A periodic volcano. *Geophys. Res. Lett.* **29**, 84–1.

Rathbun, J. A., J. R. Spencer, L. K. Tamppari, T. Z. Martin, L. Barnard, and L. D. Travis 2004. Mapping of Io's thermal radiation by the Galileo photopolarimeter-radiometer (PPR) instrument. *Icarus* **169**, 127–139.

Schenk, P., H. Hargitai, R. Wilson, A. McEwen, and P. Thomas 2001. The mountains of Io: Global and geological perspectives from Voyager and Galileo. *J. Geophys. Res.* **106**, 33201–33222.

Sinton, W. M. 1980. Io's 5 micron variability. *ApJ* **235**, L49–L51.

Sinton, W. M., A. T. Tokunaga, E. E. Becklin, I. Gatley, T. J. Lee, and C. J. Lonsdale 1980. Io - Ground-based observations of hot spots. *Science* **210**, 1015–1017.

Spencer, J. R., J. A. Rathbun, L. D. Travis, L. K. Tamppari, L. Barnard, T. Z. Martin, and A. S. McEwen 2000. Io's Thermal Emission from the Galileo Photopolarimeter- Radiometer. *Science* **288**, 1198–1201.

Spencer, J. R., M. A. Shure, M. E. Ressler, W. M. Sinton, and J. D. Goguen 1990. Discovery of hotspots on Io using disk-resolved infrared imaging. *Nature* **348**, 618–621.

van Dam, M. A., D. Le Mignant, and B. Macintosh 2004. Performance of the Keck Adaptive Optics systems. *Appl. Opt.* **43**, 5458–5467.

Veeder, G. J., D. L. Matson, T. V. Johnson, D. L. Blaney, and J. D. Goguen 1994. Io's heat flow from infrared radiometry: 1983-1993. *J. Geophys. Res.* **99**, 17095–17162.

Veeder, G. J., D. L. Matson, T. V. Johnson, A. G. Davies, and D. L. Blaney 2004. The polar contribution to the heat flow of Io. *Icarus* **169**, 264–270.

Williams, D. A., A. G. Davies, L. P. Keszthelyi, and R. Greeley 2001. The summer 1997 eruption at Pillan Patera on Io: Implications for ultrabasic lava flow emplacement. *J. Geophys. Res.* **106**, 33105–33120.

Wizinowich, P., D. S. Acton, C. Shelton, P. Stomski, J. Gathright, K. Ho, W. Lupton, K. Tsubota, O. Lai, C. Max, J. Brase, J. An, K. Avicola, S. Olivier, D. Gavel, B. Macintosh, A. Ghez, and J. Larkin 2000. First Light Adaptive Optics Images from the Keck II Telescope: A New Era of High Angular Resolution Imagery. *PASP* **112**, 315–319.

Figures

Tables
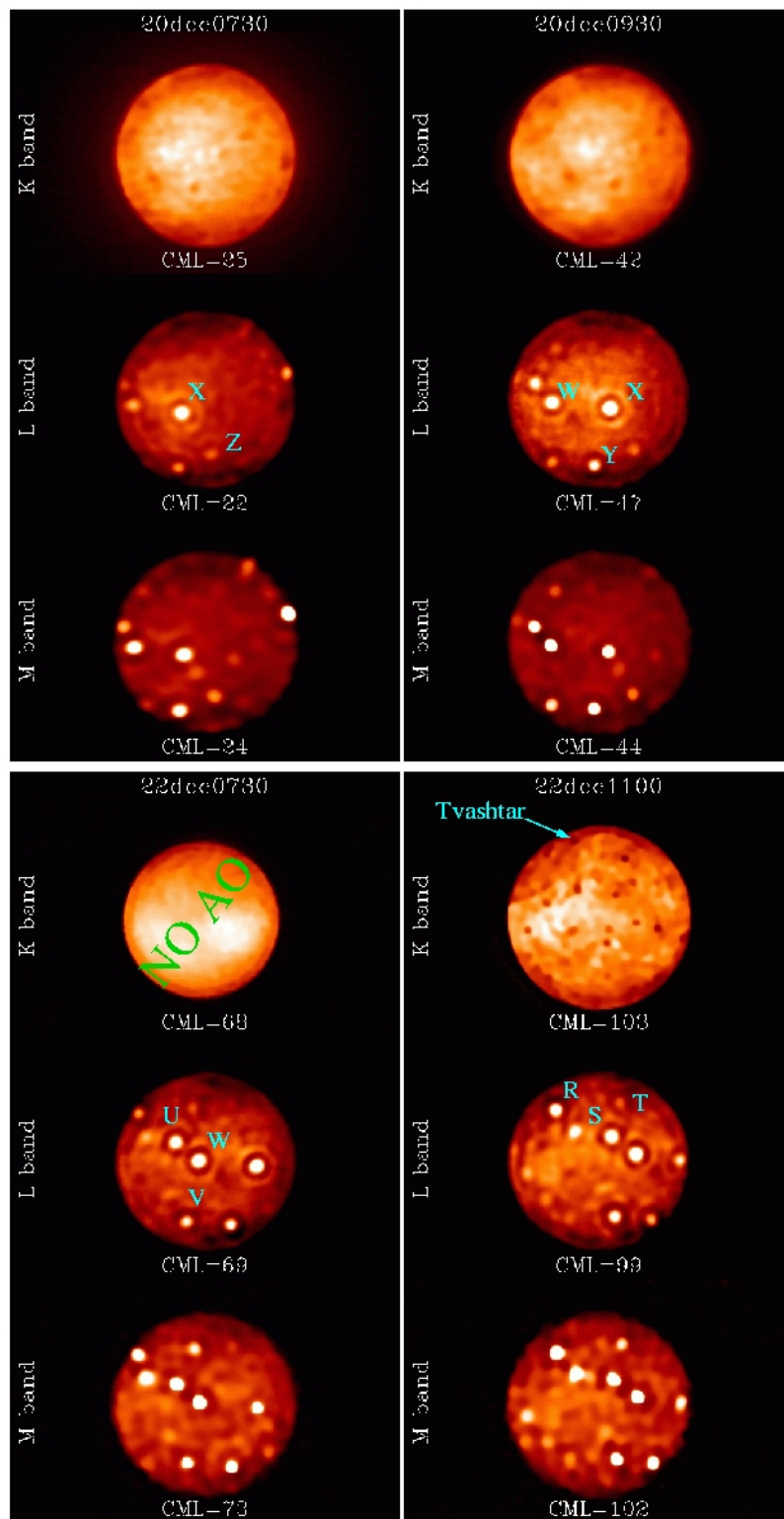
Fig. 1a.— Kc, Lp, and Ms images deconvolved. Upper-left: 20dec0730, CML~25; Upper-right: 20dec0930, CML~45; Lower-left: 22dec0730, CML~70; Lower-right: 22dec1100, CML~100.
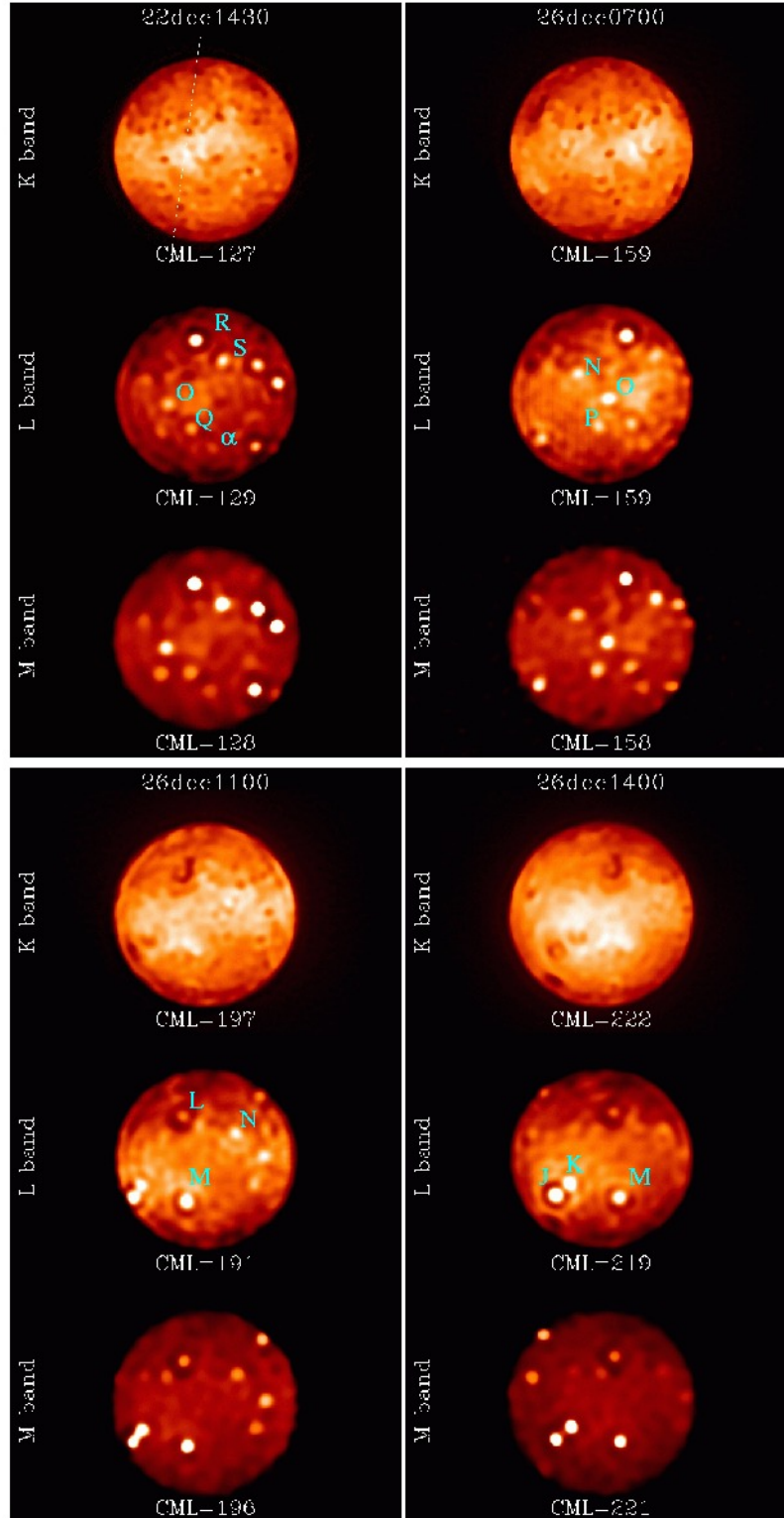
Fig. 1b.— Kc, Lp, and Ms band images deconvolved. Upper-left: 22dec1430, CML~130; Upper-right: 26dec0700, CML~160; Lower-left: 26dec1100, CML~200; Lower-right:
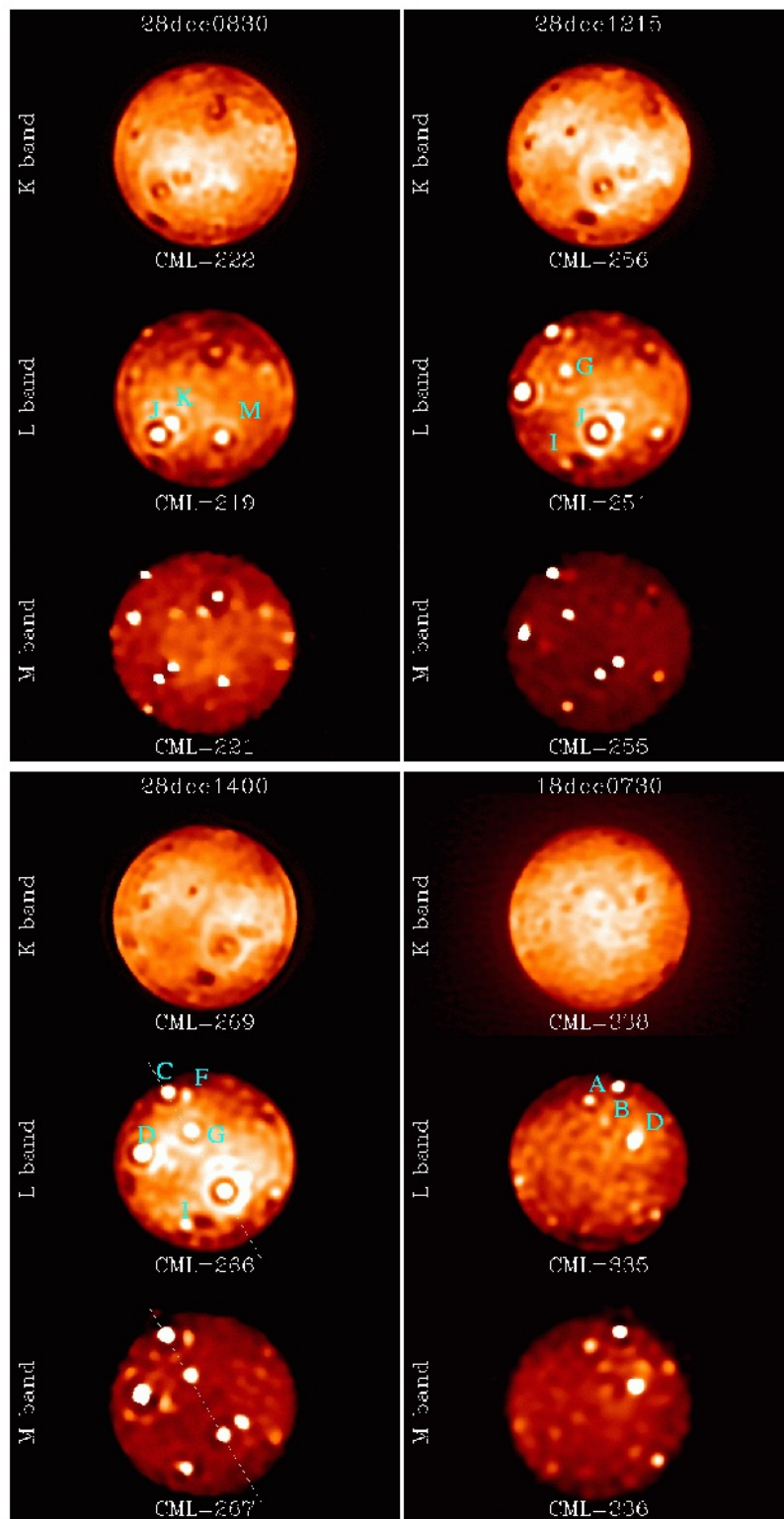
Fig. 1c.— Kc, Lp, and Ms images deconvolved. Upper-left: 28dec0830, CML∼220; Upper-right: 28dec1215, CML∼255; Lower-left: 28dec1400, CML∼270; Lower-right: 18dec0730, CML∼340. A set of last images, the 28dec1400 L- and Ms-images, is displayed in Fig.

Fig. 2a.— Cut-Profile of the 22dec1430 Kc image.

Profile on K band 22dec1430 image
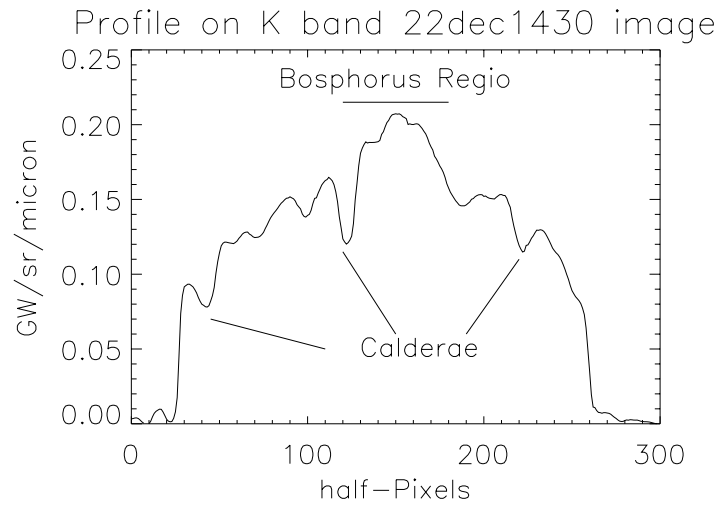
Fig. 2b.— Cut-Profile on 28dec1400 Lp and Ms images.
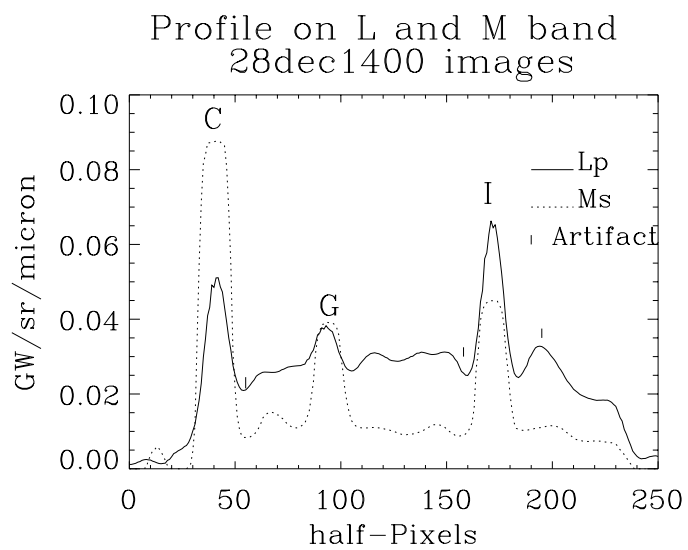
Fig. 3.— Cylindrical maps in Kc, Lp and Ms bands. The Kc map was obtained through 11 observations. Twelve images were used to build the Lp and Ms maps. The 6-pixel edge of each strip is a mean of two adjacent strips. Top image: Kc map; Middle: Lp map and bottom: Ms map.
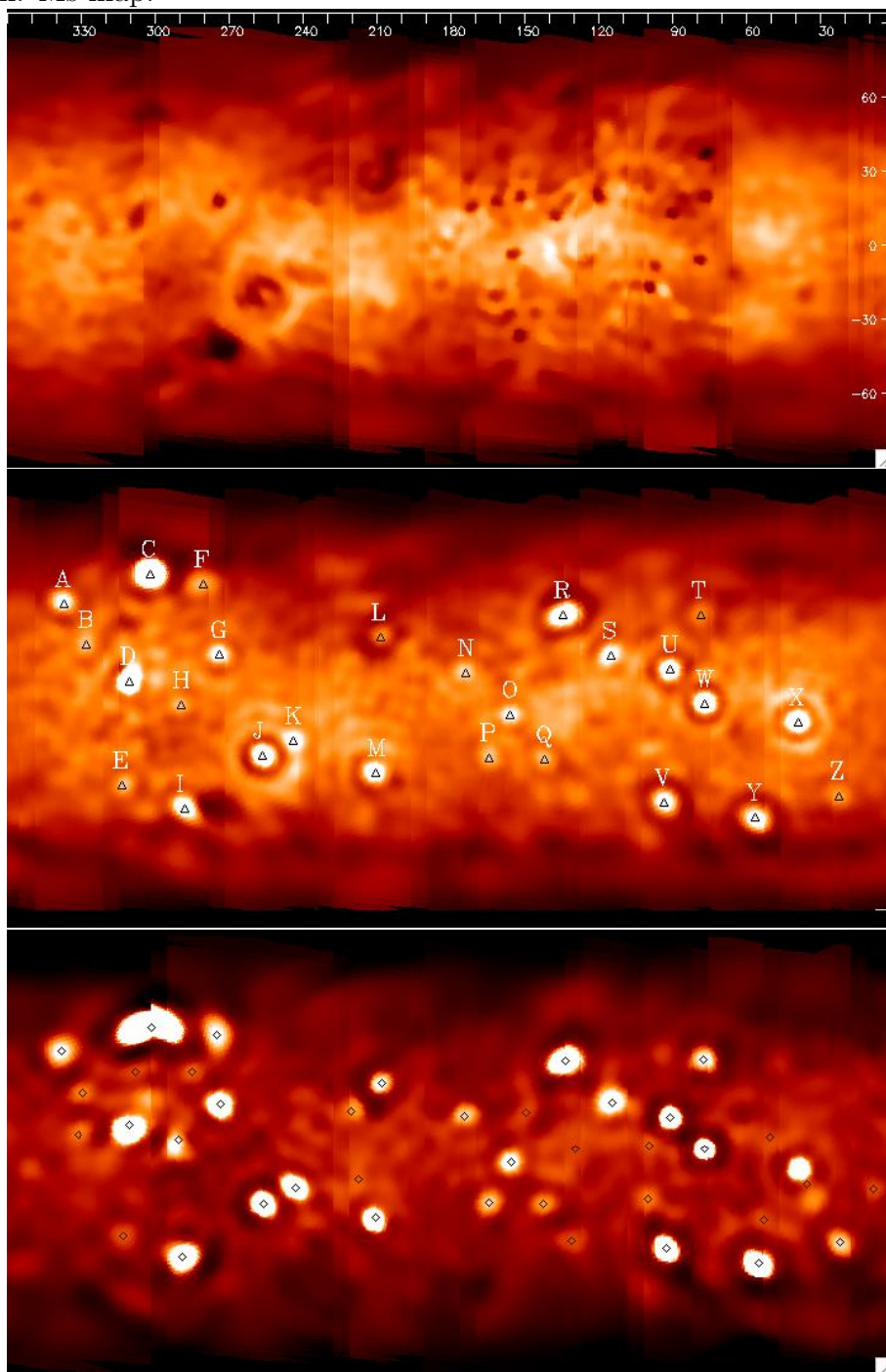
Fig. 4a.— Comparison of the position of the 16 hot spots (A to P) detected with SSI surface data.

-A-Surt
(41N ,337W)

-B-Fuchi
(25N ,328W)

-C-Dazhbog
(53N ,302W)

-D-Loki
(10N ,311W)

-E-Songon
(32S 314W)

-F-Unnamed
(49N ,281W)

-C-Dacdalus
(20N ,274W)

-H-Hephaestus
(0N ,28EW)

-I-Ulgon
(42S 283W)

-J-Polo
(20S ,257W)

-K-Pillan
(14S ,244W)

-L-Isum
(28N ,209W)

-M-Marduk

-N-Zamama

-O-Promethous

-P-Culann
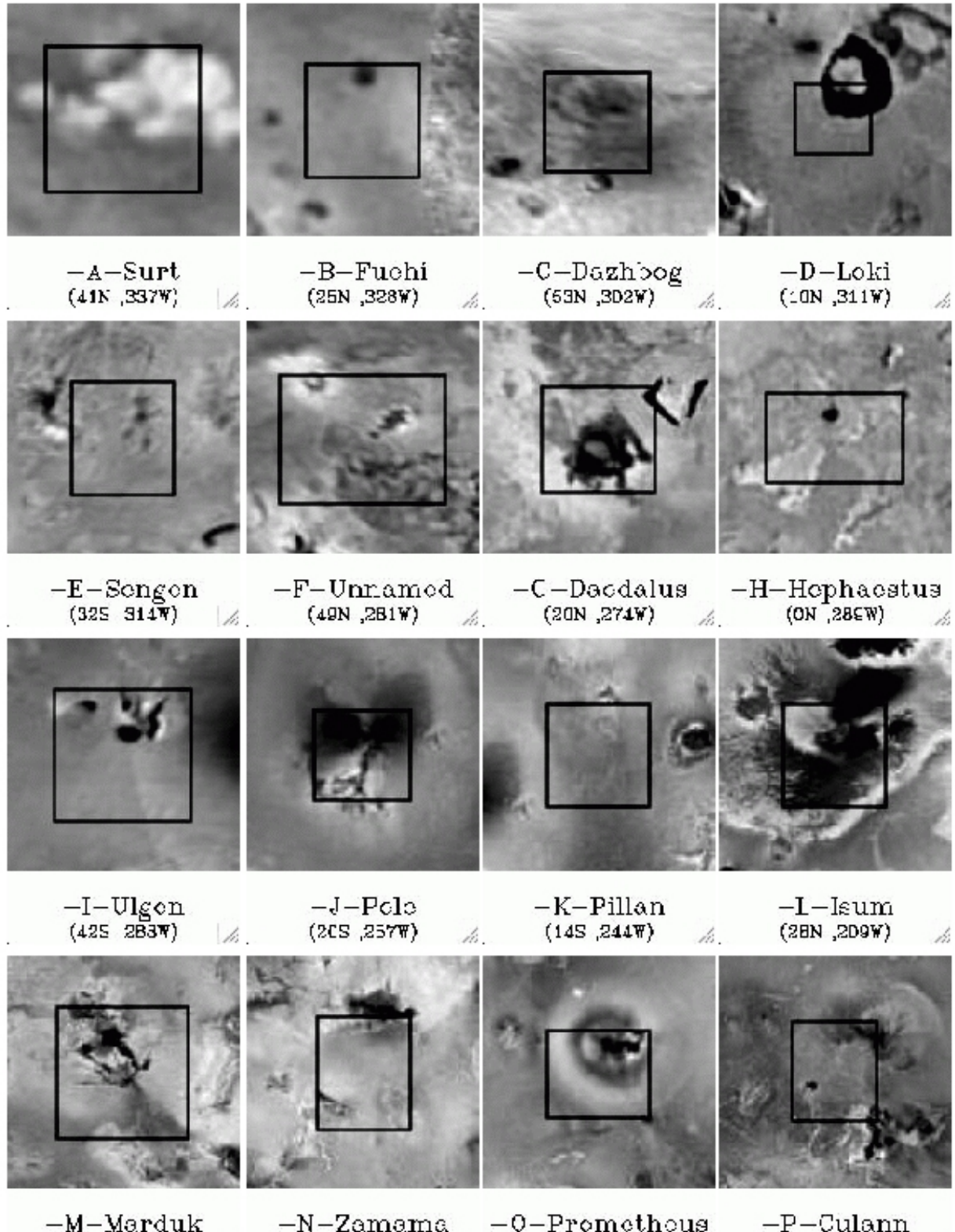
Fig. 4b.— Comparison of the position of the last 10 hot spots (Q to Z) detected with SSI surface data.

-Q-Tupan
(22S 142W)

-R-Thor
(36N ,135W)

-S-Amirani
(20N ,115W)

-T-Zal
(36N ,78W)

-U-Gish Bar
(14N ,91W)

-V-Unnamed
(40S ,84W)

-W-Tawhaki
(0N ,77W)

-X-Janus
(7S ,33W)

-Y-Masubi
(45S ,57W)

-Z-Uta
(37S ,23W)
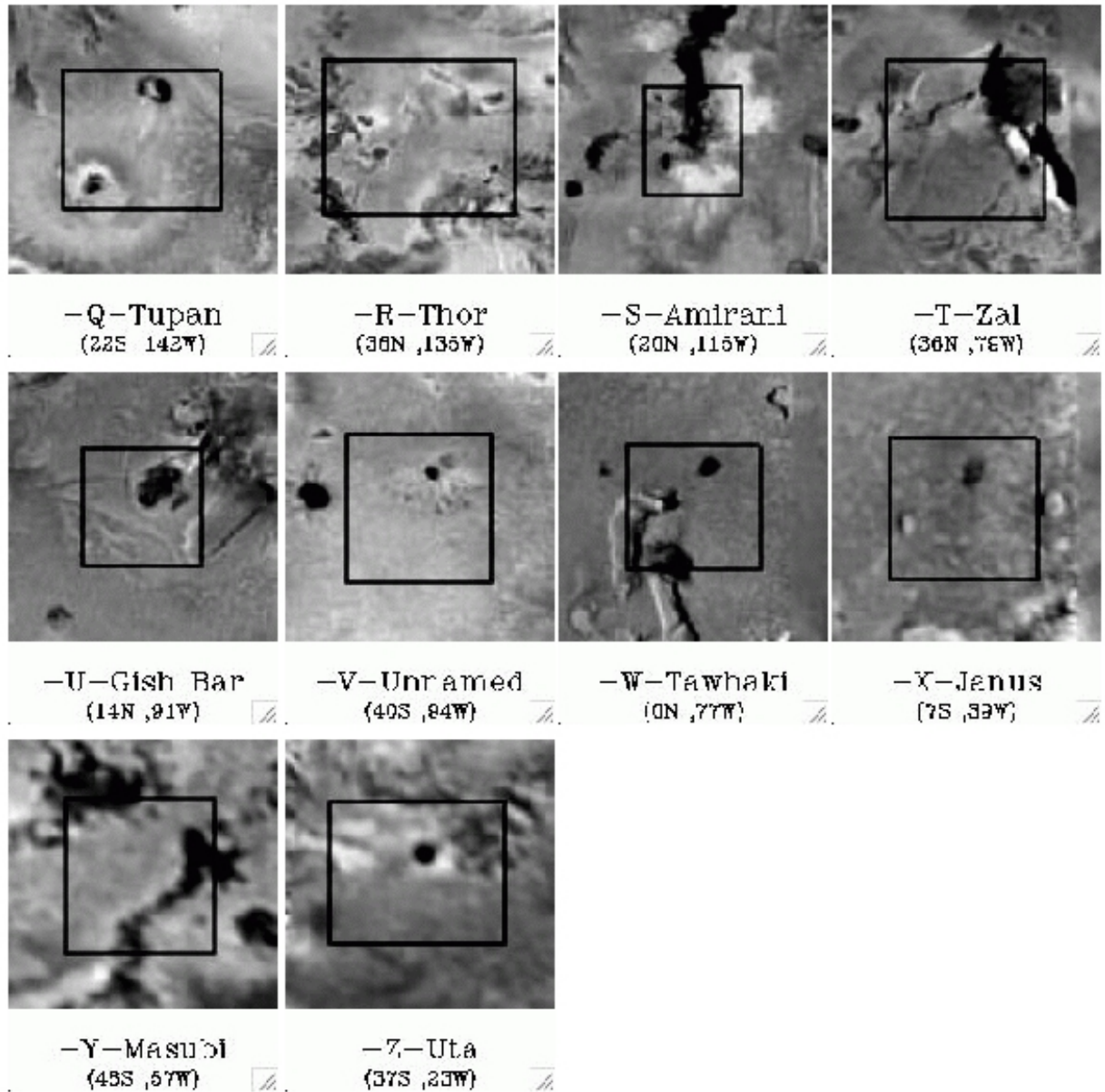
Fig. 5.— Fit of the Davies 1996 model to our data produces a range of temperatures and areas. This figure shows the model output from fits to the Pele and Isum data. With a model temperature binsize of 1 K, the combined output of the thermal emission from all of the areas at different temperatures reproduce the observed thermal emission. Cooling times are also shown; the coolest material is the oldest. For comparison, other temperature-area distributions are shown for several volcanoes observed by Galileo NIMS in June 1996 (Davies *et al.* 2000): (1) Gish Bar, (2) Prometheus, (3) Malik and (4) Monan. The massive Surt eruption of 2001 (Marchis *et al.* 2002) stands out with its very high temperature distribution and relatively large areas at these temperatures, a mark of the violence of the eruption.
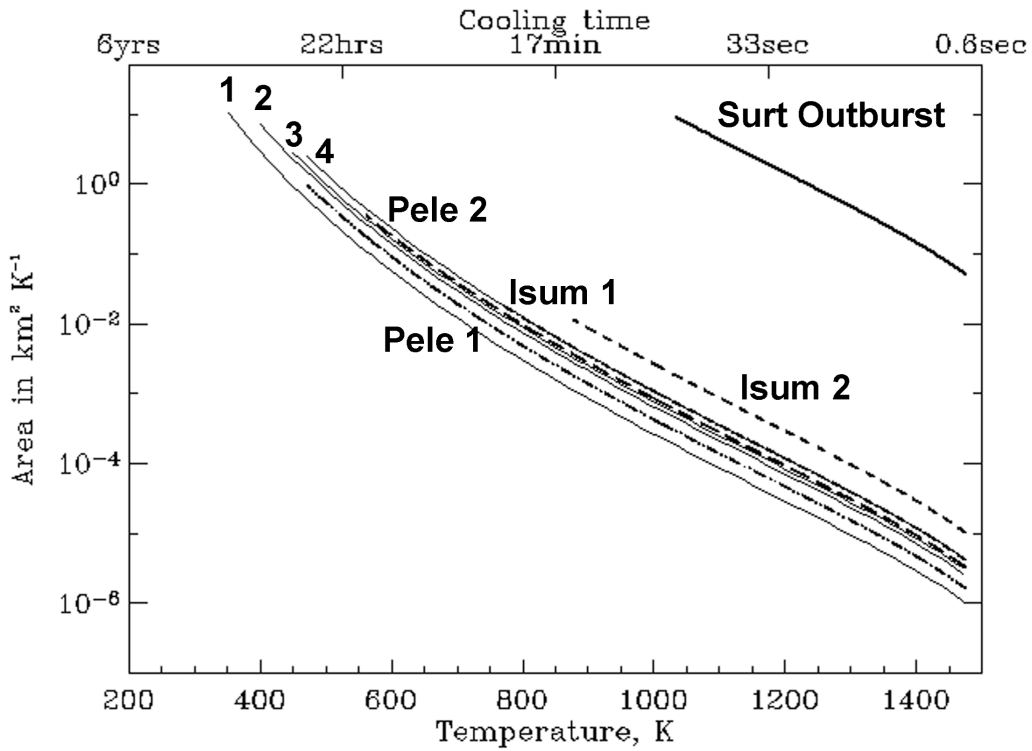
Fig. 6.— Total output of 26 detected volcanoes based on the one-temperature blackbody fit of their Lp and Ms intensity measurements. Loki and Dazhbog eruptive centers represent 36% and 16% of the total output of Io in December 2001. Both hot spot are localized on the same hemisphere of Io.

Table 1a: Quality and Photometry measured from PSF stars and photometric stars.

Star name	date	band	airmass	FWHM	SR[1]	total Int. time	Flux[2]	Δ flux	Z_0[3]	ΔZ_0
HIP30769	18dec0730	Kcont	1.25	56.4	0.29	6	8.242E6	255000		
HIP30769	18dec0730	Lp	1.23	81.7	0.53	0.55	5.095E6	78800		
HIP30769	18dec0730	Lp	1.62	83.8	0.42	0.55	4.204E6	145000		
HD22686	18dec0730	Kcont	1.32	413.1	0.00	20	9.309E6	188000	21.38	0.02
HD22686	18dec0730	Ks	1.47	520.7	0.00	5	2.556E7	1.37E6		
HD22686	18dec0730	Lp	1.26	147.2	0.05	3	9.390E6	310000	23.47	0.04
HD22686	18dec0730	Ms	1.23	55.7	0.02	11	3.982E6	322442	21.22	0.09
HIP33649	18dec0930	Kcont	1.14	51.9	0.14	5	1.019E6	135200		
HIP33649	18dec0930	Kp	1.13	61.5	0.18	5	1.611E7	3.13E6		
HIP33277	18dec0930	Lp	1.07	84.3	0.65	0.9	4.232E7	275000		
HD22686	20dec0730	Kcont	1.07	570.0	0.00	20	1.215E7	1.70E6	21.65	0.15
HD22686	20dec0730	Lp	1.07	370.0	0.02	10	3.582E7	3.32E6	23.60	0.10
HD22686	20dec0730	Ms	1.06	0.00	0.02	11	5.372E6	590699	21.53	0.12
HIP30769	20dec0730	Kcont	1.32	60.1	0.16	6	9.566E6	560726	21.54	0.06
HIP33277	20dec0730	Ms	1.37	110.4	0.31	0.55	3.263E6	80000		
HIP30769	20dec0930	Kcont	1.04	55.7	0.22	2	2.929E6	201800	21.44	0.07
HIP33277	22dec0730	Kcont	1.28	50.9	0.36	0.3	2.175E6	58500		
HIP33277	22dec0730	Lp	1.34	82.8	0.73	0.18	8.861E6	118260		
HIP33277	22dec0730	Ms	1.31	97.5	0.39	0.18	1.254E6	34000		
HD40335	22dec0730	Lp	1.12	137.9	0.08	1.65	1.265E7	359372	23.71	0.03
HD40335	22dec0730	Kcont	1.14	250.0	0.02	20	2.460E7	226000	21.71	0.01
HD40335	22dec0730	Ms	1.12	110.0	0.07	1.65	1.257E6	58600	21.23	0.05
HIP33277	22dec1100	Kcont	1.01	49.8	0.56	3	2.380E7	152500		
HIP33277	22dec1100	Ms	1.01	97.6	0.70	4	2.980E7	311000		
HIP33277	22dec1100	Lp	1.01	83.0	0.76	5.4	2.907E8	2.25E6		
HIP33277	22dec1430	Kcont	1.48	51.4	0.42	3	2.171E7	36400		
HIP33277	22dec1430	Lp	1.51	83.2	0.69	5.4	2.551E8	1.55E6		
HIP33277	22dec1430	Ms	1.54	99.5	0.58	4	2.515E7	448600		
HIP33277	23dec1100	Lp	1.00	82.0	0.67	3.006	1.205E8	9.65E6	23.62	0.03
HD40335	23dec1100	Lp	1.11	151.3	0.11	3	2.114E7	425800		
HIP33277	26dec0700	Kcont	1.59	51.0	0.41	3	2.238E7	433200		
HIP33277	26dec0700	Lp	1.56	83.2	0.72	5.4	2.622E8	3.39E6		
HIP30769	26dec0700	Lp	1.22	79.6	0.72	5.4	5.651E7	866000		
HIP33277	26dec0700	Ms	1.53	97.9	0.65	4	2.573E7	989000		

Table 1b: Quality and Photometry measured from PSF stars and photometric stars.

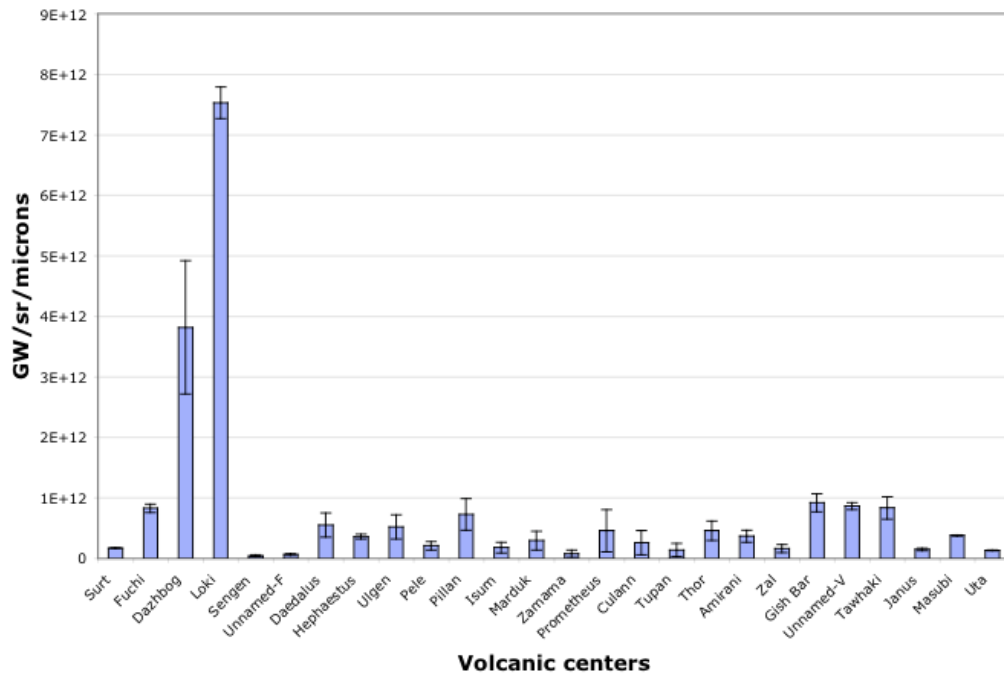| Star name	date	band	airmass	FWHM	SR[1]	total Int. time	Flux[2]	Δ flux	Z_0[3]	ΔZ_0
HIP33277	26dec1100	Kcont	1.00	51.3	0.43	3	2.527E7	254000		
HIP33277	26dec1100	Lp	1.00	82.9	0.74	5.4	2.981E8	3.25E6		
HIP30769	26dec1100	Lp	1.04	81.2	0.68	2.65	2.712E7	676500		
HIP33277	26dec1100	Ms	1.00	97.7	0.67	4	2.963E7	786000		
HD40335	26dec1100	Lp	1.18	153.0	0.09	3	2.028E7	560500	23.57	0.03
HD40335	26dec1100	Ms	1.19	102.0	0.06	1.65	1.493E6	135000	21.49	0.10
HD40335	26dec1100	Kcont	1.17	275.7	0.02	20	2.190E7	510000	21.59	0.03
HIP30769	26dec1400	Kcont	1.37	52.8	0.37	10	1.627E7	513500		
HIP30769	26dec1400	Lp	1.44	79.8	0.71	5.4	5.785E7	455500		
HIP30769	26dec1400	Ms	1.47	97.5	0.31	4	5.215E6	400000		
HIP30769	28dec0830	Kcont	1.04	52.9	0.18	3	4.681E6	456700		
HIP30769	28dec0830	Lp	1.03	79.2	0.75	5.4	5.979E7	611800		
HD40335	28dec0830	Lp	1.05	112.6	0.15	3	2.076E7	522000	23.60	0.03
HD40335	28dec0830	Kcont	1.05	276.1	0.02	14	1.409E7	670500	21.49	0.05
HD40335	28dec0830	Ms	1.05	87.4	0.06	1.65	1.482E6	080000	21.47	0.06
HIP30769	28dec0830	Ms	1.04	98.0	0.34	4	5.942E6	885000		
HIP30769	28dec1215	Kcont	1.25	51.9	0.20	2.5	4.990E6	380000		
HIP30769	28dec1215	Lp	1.27	80.3	0.61	5.4	6.560E7	2.69E6		
HD40335	28dec1215	Lp	1.23	193	0.05	3	1.772E7	1.62E6	23.42	0.10
HD40335	28dec1215	Ms	1.27	124.5	0.04	10	7.242E6	390000	21.26	0.06
HD40335	28dec1215	Kcont	1.22	354	0.01	12	9.717E6	1.23E6	21.25	0.14
HIP30769	28dec1215	Ms	1.28	97.5	0.33	3.6	5.441E6	387000		
HIP34861	28dec1400	Kcont	1.45	54.2	0.33	50	3.097E7	1.22E6		
HIP34861	28dec1400	Lp	1.52	81.4	0.60	18	7.552E7	2.31E6		
HD77281	28dec1400	Lp	1.33	116.2	0.11	3	1.033E7	649000	23.42	0.07
HD77281	28dec1400	Kcont	1.31	291.3	0.02	20	1.153E7	1.05E6	21.47	0.10
HD77281	28dec1400	Ms	1.36	117.2	0.07	10	5.134E6	359000	21.74	0.08
HIP34861	28dec1400	Ms	1.57	98.9	0.28	16	8.876E6	1.27E6		

1. SR (Strehl Ratio) measurement of AO data quality

2. Flux, Δflux: integrated Flux, uncertainty on Flux

3. Z_o, ΔZ_o: Zero-point and uncertainty on Zero-point

Table 2a: Summary of the observational circumstances and photometry of the Io data set.

Name	Filter	Total Int. GW/sr/μm	Magnitude	Background Int. GW/sr/μm	Time UT	Airmass	Ind. Integ. Time	Coadds #frames	CML[1] deg	% hot spot[2]
18dec0730	Kcont	10802.	3.02	0.0084 +/-0.0027	07:48:41.39	1.58	1.000	3	337.5	
18dec0730	Lp	893.	3.44	0.0001 +/-0.0003	07:29:01.03	1.75	0.055	50	334.6	3%
18dec0730	Ms	550.	3.04	0.0015 +/-0.0015	07:36:28.73	1.68	0.055	100	335.6	16%
18dec0930	Kcont	10922.	3.01	0.0065 +/-0.0028	09:02:20.97	1.20	1.000	3	347.6	
18dec0930	Lp	840.	3.51	0.0010 +/-0.0004	08:54:48.61	1.23	0.055	50	351.6	
18dec0930	Ms	571.	3.00	0.0029 +/-0.0030	08:59:31.76	1.21	0.055	50	347.4	
20dec0730	Kcont	6267.	3.61	0.0053 +/-0.0009	07:54:49.52	1.48	2.000	2	25.4	
20dec0730	Lp	780.	3.59	0.0004 +/-0.0002	07:33:43.91	1.63	0.055	50	21.8	2%
20dec0730	Ms	462	3.23	0.0004 +/-0.0005	07:45:04.42	1.54	0.055	100	24.1	8%
20dec0930	Kcont	6256.	3.61	0.0050 +/-0.0009	09:51:12.52	1.07	2.000	2	41.9	
20dec0930	Lp	844.	3.50	0.0002 +/-0.0002	10:11:52.03	1.04	0.055	50	47.3	2%
20dec0930	Ms	433.	3.30	0.0000 +/-0.0010	10:02:50.12	1.05	0.055	50	43.5	7%
22dec0730	Kcont	6417.	3.59	0.0004 +/-0.0009	07:24:21.72	1.63	2.000	2	68.4	
22dec0730	Lp	805.	3.55	0.0001 +/-0.0002	07:48:26.33	1.46	0.055	50	69.1	3%
22dec0730	Ms	621.	2.91	0.0012 +/-0.0013	07:55:30.18	1.42	0.055	50	72.8	9%
22dec1100	Kcont	6240.	3.62	0.0015 +/-0.0012	11:25:32.06	1.00	2.000	2	102.5	
22dec1100	Lp	862.	3.48	0.0000 +/-0.0004	11:11:46.26	1.00	0.055	50	98.8	3%
22dec1100	Ms	640.	2.88	0.0011 +/-0.0014	11:19:03.71	1.00	0.055	50	101.6	8%
22dec1430	Kcont	6195.	3.63	0.0023 +/-0.0014	14:18:03.63	1.39	2.000	2	126.9	
22dec1430	Lp	779.	3.58	0.0001 +/-0.0003	14:31:03.03	1.46	0.055	50	128.5	2%
22dec1430	Ms	640.	3.08	0.0000 +/-0.0013	14:25:48.18	1.43	0.055	50	128.0	8%
23dec1100	Lp	957.	3.37	0.0000 +/-0.0004	11:00:57.02	1.00	0.055	50	302.5	6%
26dec0700	Kcont	6806.	3.52	0.0040 +/-0.0012	06:58:50.45	1.70	2.000	2	159.4	
26dec0700	Lp	927.	3.40	0.0003 +/-0.0004	07:00:00	1.70	0.055	50	159.4	1%
26dec0700	Ms	555.	3.03	0.0031 +/-0.0013	06:51:02.75	1.78	0.055	50	158.2	5%

Table 2b: Summary of the observational circumstances and photometry of the Io data set.

Name	Filter	Total Int. GW/sr/μm	Magnitude	Background Int. GW/sr/μm	Time UT	Airmass	Ind. Integ. Time	Coadds #frames	CML[1] deg	% hot spot[2]
26dec1100	Kcont	6856.	3.52	0.0028 +/-0.0014	11:27:58.00	1.01	2.000	2	197.4	
26dec1100	Lp	938.	3.39	0.0000 +/-0.0004	11:09:42.35	1.00	0.055	50	191.2	1%
26dec1100	Ms	478.	3.19	0.0000 +/-0.0012	11:14:53.00	1.01	0.055	50	195.6	5%
26dec1400	Kcont	6892.	3.51	0.0030 +/-0.0012	14:22:39.22	1.53	2.000	2	222.2	
26dec1400	Lp	881.	3.45	0.0001 +/-0.0004	14:07:08.71	1.43	0.055	50	218.8	1%
26dec1400	Ms	406.	3.37	0.0000 +/-0.0013	14:14:43.42	1.47	0.055	50	221.0	6%
28dec0830	Kcont	7588.	3.41	0.0025 +/-0.0015	08:50:09.19	1.12	2.000	2	222.3	
28dec0830	Lp	942.	3.38	0.0000 +/-0.0004	08:30:35.94	1.16	0.055	50	219.4	2%
28dec0830	Ms	612.	2.93	0.0024 +/-0.0011	08:42:41.04	1.13	0.055	50	221.3	6%
28dec1215	Kcont	9369.	3.18	0.0041 +/-0.0017	12:49:00.89	1.15	2.000	2	256.2	
28dec1215	Lp	1168.	3.15	0.0002 +/-0.0004	12:28:08.58	1.10	0.055	50	251.2	4%
28dec1215	Ms	600.	2.95	0.0000 +/-0.0014	12:37:31.83	1.12	0.055	50	254.5	15%
28dec1400	Kcont	7748.	3.38	0.0036 +/-0.0016	14:17:09.62	1.55	2.000	2	269.4	
28dec1400	Lp	1077.	3.24	0.0000 +/-0.0004	14:02:13.42	1.45	0.055	50	266.0	3%
28dec1400	Ms	557.	2.03	0.0000 +/-0.0011	14:07:03.07	1.48	0.055	50	267.2	20%

1. CML: Central Meridian Longitude

2. Percentage ratio of thermal output of the hotspots to solar-reflected flux

Table 3: Positions, feature candidates and comparison with previous activity reports of hot spots detected in L and M bands. Persistently active hot spots reported in Lopes-Gautier *et al.* (1999) are labeled. Three additional persistent hot spots (Fuchi, Sengen, and Daedalus) are added, based on previous ground-based AO observations taken in 1996 (Marchis *et al.* 2000), and in 1998-2000 (Marchis *et al.* 2001).

Label	position in degrees	candidate	Comments
A	40.9±6.4 N, 336.9±6.7 W	Surt	Outburst seen in Marchis *et al.* (2002)
B	24.6±5.0 N, 328.0±5.0 W	Fuchi	seen in Marchis *et al.* (2001), Persistent
C	53.0±4.3 N, 302.2±4.7 W	Dazhbog	Detected by Galileo SSI I31
D	9.70±3.1 N, 310.7±3.4 W	Loki	persistent, most energetic
E	32.4±4.9 S, 313.6±4.5 W	Sengen	seen in Marchis *et al.* (2001), Persistent
F	49.0±5.6 N, 280.6±7.3 W	Unnamed	new hot spot
G	20.3±4.6 N, 274.1±4.9 W	Daedalus	seen in Marchis *et al.* (2001), Persistent, Dark Caldera
H	0.1±4.0 N, 289.4±5.9 W	Hephaestus	see by PPR I27
I	42.1±5.8 S, 288.0±6.0 W	Ulgen	
J	20.4±4.0 S, 256.6±4.3 W	Pele	persistent, detected in K band
K	14.4±4.4 S, 243.9±4.6 W	Pillan	persistent since 1997
L	27.6±4.6 N, 208.6±4.5 W	Isum	persistent, detected in K band
M	27.4±5.8 S, 210.4±5.7 W	Marduk	persistent
N	12.8±5.0 N, 173.8±4.2 W	Zamama	
O	4.00±3.9 S, 155.8±4.5 W	Prometheus	persistent
P	21.3±4.3 S, 164.6±3.8 W	Culann	persistent
Q	22.1±5.2 S, 141.9±5.9 W	Tupan	persistent
R	36.4±5.9 N, 134.7±7.2 W	Malik-Thor	persistent
S	20.0±4.1 N, 115.2±3.8 W	Amirani	
T	36.3±6.0 N, 78.6±6.0 W	Zal	persistent
U	14.3±4.5 N, 91.1±4.5 W	Gish Bar	persistent
V	39.5±5.6 S, 93.5±5.5 W	Unnamed	Close to Arusha
W	0.4±4.7 N, 77.1±5.1 W	Tawhaki	Persistent, seen by NIMS/SSI I31
X	7.00±5.3 S, 39.2±5.6 W	Janus	Persistent
Y	45.5±5.9 S, 56.5±5.7 W	Masubi	seen during I31
Z	36.8±5.4 N, 22.5±6.7 W	Uta	

Table 4a: Corrected radiance measurements, FWHM estimates and candidates of the hot spots identified in each data set.

Hot Spot Label	Intensity in Lp in GW/sr/μm	Intensity in Ms in GW/sr/μm	FWHM in L in mas	FWHM in Ms in mas	Lp angle corr. in deg	Ms angle corr. in deg	Hot Spot Name
18dec0730A	2.5 ± 0.0	4.7 ± 0.4	56	62	39.1	39.1	Surt
18dec0730C	12.4 ± 0.6	37.1 ± 1.2	36	34	58.1	58.5	Dazhbog
18dec0730D	14.8 ± 0.5	45.1 ± 1.0	37	40	25.1	26.0	Loki
18dec0730E	1.1 ± 0.1	1.5 ± 0.2	57	63	39.5	39.9	Sengen
18dec0730G	1.0 ± 0.2	4.2 ± 0.3	44	59	62.2	63.1	Daedalus
18dec0730I	3.5 ± 0.5	7.6 ± 0.4	53	52	60.3	60.9	Ulgen
18dec0730J	0.9 ± 0.2	3.1 ± 0.2	35	54	78.9	79.8	Pele
18dec0730X	2.3 ± 0.2	2.3 ± 0.4	44	65	64.9	63.9	Janus
18dec0730Z	1.4 ± 0.1	3.1 ± 0.4	52	61	58.4	57.7	Uta
20dec0730B	0.6 ± 0.1	2.2 ± 0.2	51	75	57.0	59.1	Fuchi
20dec0730C	1.2 ± 0.9	22.7 ± 4.7	24	53	83.5	84.9	Dazhbog
20dec0730D	4.3 ± 0.4	30.1 ± 0.6	56	45	71.3	73.6	Loki
20dec0730U	1.3 ± 0.3	7.1 ± 0.5	58	53	69.8	67.6	Gish Bar
20dec0730W	2.4 ± 0.2	10.4 ± 0.3	61	52	55.3	53.0	Tawhaki
20dec0730X	3.4 ± 0.1	5.7 ± 0.5	61	53	19.4	17.4	Janus
20dec0730Y	2.5 ± 0.3	9.0 ± 1.2	49	52	56.1	55.1	Masubi
20dec0730Z	0.9 ± 0.2	3.3 ± 0.3	51	60	38.6	38.6	Uta
20dec0930A	1.0 ± 0.3	1.9 ± 0.3	49	52	74.9	72.0	Surt
20dec0930T	1.1 ± 0.1	2.3 ± 0.1	56	56	45.2	47.6	Zal
20dec0930U	3.1 ± 0.1	6.5 ± 0.1	59	42	45.2	48.8	Gish Bar
20dec0930V	3.0 ± 0.3	7.6 ± 0.2	52	47	58.7	61.1	Unnamed-V
20dec0930W	4.1 ± 0.1	9.1 ± 0.1	60	39	29.8	33.6	Tawhaki
20dec0930X	4.5 ± 0.5	5.2 ± 0.0	49	40	11.9	9.8	Janus
20dec0930Y	3.5 ± 0.2	7.7 ± 0.2	46	41	48.0	48.7	Masubi
20dec0930Z	1.2 ± 0.1	2.8 ± 0.2	52	51	44.8	43.2	Uta
22dec0730R	4.8 ± 0.5	10.4 ± 1.0	52	50	70.1	67.2	Thor
22dec0730S	1.5 ± 0.4	5.0 ± 0.8	61	63	48.8	45.4	Amirani
22dec0730T	1.1 ± 0.0	2.9 ± 0.2	51	50	35.6	34.9	Zal
22dec0730U	3.5 ± 0.3	9.8 ± 0.1	55	40	25.1	22.0	Gish Bar
22dec0730V	3.3 ± 0.2	8.6 ± 0.4	48	33	46.8	45.4	Unnamed-V
22dec0730W	4.7 ± 0.3	13.0 ± 0.3	49	41	8.1	4.5	Tawhaki
22dec0730X	6.0 ± 0.6	7.4 ± 0.2	46	34	31.1	34.6	Janus
22dec0730Y	4.6 ± 0.3	8.7 ± 0.3	47	37	48.6	49.4	Masubi
22dec0730Z	0.8 ± 0.2	2.7 ± 0.3	54	57	57.5	60.1	Uta

Table 4b: Corrected radiance measurements, FWHM estimates and candidates of the hot spots identified in each data set.

Hot Spot Label	Intensity in Lp in GW/sr/μm	Intensity in Ms in GW/sr/μm	FWHM in L in mas	FWHM in Ms in mas	Lp angle corr. in deg	Ms angle corr. in deg	Hot Spot Name
22dec1100N	1.2 ± 0.4	0.6 ± 0.3	40	54	75.3	72.5	Zamama
22dec1100O	1.8 ± 0.3	4.4 ± 0.5	55	65	57.2	54.4	Prometheus
22dec1100Q	1.4 ± 0.2	1.8 ± 0.2	57	55	48.1	45.8	Tupan
22dec1100R	6.2 ± 0.1	12.1 ± 0.4	43	44	48.2	46.4	Thor
22dec1100S	1.8 ± 0.2	4.1 ± 0.6	52	47	24.3	22.6	Amirani
22dec1100T	0.9 ± 0.1	2.6 ± 0.2	48	45	39.3	40.6	Zal
22dec1100U	3.7 ± 0.4	10.0 ± 0.2	52	39	14.6	16.3	Gish Bar
22dec1100V	3.7 ± 0.2	0.0 ± 0.0	50	39	41.6	42.0	Unnamed-V
22dec1100W	5.5 ± 0.0	13.1 ± 0.1	41	38	21.7	24.5	Tawhaki
22dec1100X	3.4 ± 0.1	5.1 ± 0.2	50	49	60.0	62.8	Janus
22dec1430N	0.7 ± 0.2	1.8 ± 0.3	50	69	46.3	46.8	Zamama
22dec1430O	1.3 ± 0.2	3.0 ± 0.4	51	51	27.9	28.4	Prometheus
22dec1430P	0.9 ± 0.1	3.1 ± 0.0	58	69	42.0	42.4	Culann
22dec1430Q	1.1 ± 0.1	2.4 ± 0.3	47	60	27.2	27.5	Tupan
22dec1430R	5.3 ± 0.2	10.6 ± 0.0	44	42	35.1	35.2	Thor
22dec1430S	1.7 ± 0.0	4.3 ± 0.4	56	54	22.4	22.1	Amirani
22dec1430U	2.8 ± 0.1	8.5 ± 0.4	57	44	39.1	38.7	Gish Bar
22dec1430V	3.4 ± 0.1	8.5 ± 0.4	51	44	52.0	51.8	Unnamed-V
22dec1430W	4.8 ± 0.4	10.8 ± 0.4	53	42	51.4	50.9	Tawhaki
22dec1430Y	2.0 ± 0.5	3.2 ± 0.6	37	38	77.9	77.6	Masubi
23dec1100A	3.8 ± 0.2	N/A	60	38	50.2	50.2	Surt
23dec1100B	0.9 ± 0.1	N/A	57	38	33.7	33.7	Fuchi
23dec1100C	17.0 ± 0.3	N/A	37	38	51.2	51.2	Dazhbog
23dec1100D	23.4 ± 1.2	N/A	39	38	11.4	11.4	Loki
23dec1100E	1.3 ± 0.1	N/A	59	38	35.8	35.8	Sengen
23dec1100F	2.6 ± 0.4	N/A	53	38	50.9	50.9	Unnamed-F
23dec1100G	2.4 ± 0.1	N/A	66	38	33.5	33.5	Daedalus
23dec1100H	1.0 ± 0.0	N/A	63	38	13.2	13.2	Hephaestus
23dec1100I	4.1 ± 0.5	N/A	58	38	45.8	45.8	Ulgen
23dec1100J	6.1 ± 0.2	N/A	45	38	49.9	49.9	Pele
23dec1100K	2.5 ± 0.6	N/A	44	38	60.0	60.0	Pillan

Table 4c: Corrected radiance measurements, FWHM estimates and candidates of the hot spots identified in each data set.

Hot Spot Label	Intensity in Lp in GW/sr/μm	Intensity in Ms in GW/sr/μm	FWHM in L in mas	FWHM in Ms in mas	angle corr. in deg	angle corr. in deg	Hot Spot Name
26dec0700M	3.1 ± 0.3	6.5 ± 0.4	59	55	56.7	57.7	Marduk
26dec0700N	1.3 ± 0.3	2.4 ± 0.4	59	59	18.0	19.0	Zamama
26dec0700O	1.5 ± 0.1	3.1 ± 0.3	57	53	6.8	6.3	Prometheus
26dec0700P	1.4 ± 0.1	2.6 ± 0.4	58	56	23.7	23.9	Culann
26dec0700Q	1.0 ± 0.1	1.8 ± 0.2	60	54	29.3	28.7	Tupan
26dec0700R	4.9 ± 0.5	9.2 ± 0.4	50	38	41.6	41.0	Thor
26dec0700S	1.3 ± 0.2	4.4 ± 0.1	63	61	47.1	46.0	Amirani
26dec0700U	0.4 ± 0.2	4.5 ± 0.3	41	48	68.8	67.7	Gish Bar
26dec0700V	0.6 ± 0.4	4.4 ± 0.4	34	48	72.1	71.3	Unnamed-V
26dec0700W	0.4 ± 0.7	1.9 ± 0.4	49	45	82.3	81.1	Tawhaki
26dec1100J	8.9 ± 0.6	7.4 ± 0.9	49	42	67.3	63.3	Pele
26dec1100K	1.8 ± 0.3	6.5 ± 0.5	46	52	54.4	50.3	Pillan
26dec1100L	1.1 ± 0.1	2.0 ± 0.1	53	49	30.8	28.7	Isum
26dec1100M	3.7 ± 0.3	6.0 ± 0.1	59	44	34.5	32.4	Marduk
26dec1100N	1.2 ± 0.2	2.1 ± 0.3	57	56	20.5	24.3	Zamama
26dec1100O	1.4 ± 0.1	3.3 ± 0.3	57	61	35.8	40.2	Prometheus
26dec1100P	1.0 ± 0.1	2.5 ± 0.3	50	66	34.7	38.0	Culann
26dec1100R	2.4 ± 0.4	6.8 ± 0.3	48	46	63.0	66.4	Thor
26dec1400C	7.4 ± 0.6	26.0 ± 0.6	44	41	85.9	84.5	Dazhbog
26dec1400G	1.0 ± 0.2	4.3 ± 0.3	54	58	57.3	55.3	Daedalus
26dec1400J	7.1 ± 0.7	6.8 ± 0.4	48	42	43.0	41.2	Pele
26dec1400K	2.5 ± 0.1	6.1 ± 0.2	52	43	29.6	27.8	Pillan
26dec1400L	1.0 ± 0.1	2.0 ± 0.1	52	47	27.6	28.4	Isum
26dec1400M	3.1 ± 0.1	4.6 ± 0.1	61	45	30.3	30.9	Marduk
26dec1400N	0.7 ± 0.2	0.8 ± 0.2	43	53	46.0	48.2	Zamama
28dec0830C	10.1 ± 0.7	36.5 ± 2.1	44	26	85.5	84.3	Dazhbog
28dec0830G	1.0 ± 0.1	7.5 ± 0.1	56	55	56.8	55.0	Daedalus
28dec0830J	8.0 ± 0.4	10.4 ± 0.1	44	28	42.5	40.9	Pele
28dec0830K	3.3 ± 0.3	8.8 ± 0.1	56	29	29.1	27.6	Pillan
28dec0830L	1.5 ± 0.1	3.6 ± 0.1	59	38	27.8	28.6	Isum
28dec0830M	3.9 ± 0.1	7.2 ± 0.1	62	34	30.4	31.0	Marduk
28dec0830N	1.4 ± 0.5	2.1 ± 0.1	52	60	46.6	48.5	Zamama

Table 4d: Corrected radiance measurements, FWHM estimates and candidates of the hot spots identified in each data set.

Hot Spot Label	Intensity in Lp in GW/sr/μm	Intensity in Ms in GW/sr/μm	FWHM in L in mas	FWHM in Ms in mas	angle corr. in deg	angle corr. in deg	Hot Spot Name
28dec1215C	12.7 ± 0.6	37.2 ± 0.1	45	36	66.8	65.1	Dazhbog
28dec1215D	28.8 ± 2.9	55.7 ± 0.5	43	37	59.8	56.6	Loki
28dec1215F	2.4 ± 0.4	3.0 ± 0.3	51	51	53.7	52.4	Unnamed-F
28dec1215G	3.1 ± 0.2	6.9 ± 0.3	73	39	29.1	26.7	Daedalus
28dec1215I	3.2 ± 0.6	7.3 ± 0.4	53	40	54.8	53.1	Ulgen
28dec1215J	9.2 ± 0.2	8.7 ± 0.3	47	36	22.8	22.3	Pele
28dec1215K	3.2 ± 0.3	8.1 ± 0.2	47	38	17.7	19.3	Pillan
28dec1215L	2.5 ± 0.1	3.2 ± 0.5	57	48	48.5	51.2	Isum
28dec1215M	3.7 ± 0.4	5.6 ± 0.5	66	47	48.6	51.2	Marduk
28dec1400C	8.6 ± 1.1	38.8 ± 1.4	44	46	59.6	59.1	Dazhbog
28dec1400D	21.9 ± 0.7	62.2 ± 2.3	41	49	45.2	44.1	Loki
28dec1400F	2.1 ± 0.3	3.6 ± 0.3	48	50	48.9	48.6	Unnamed-F
28dec1400G	2.2 ± 0.3	7.0 ± 0.5	61	49	20.1	19.7	Daedalus
28dec1400H	0.5 ± 0.1	2.6 ± 0.7	43	60	23.5	22.3	Hephaestus
28dec1400I	2.5 ± 0.7	6.5 ± 0.5	46	46	48.1	47.7	Ulgen
28dec1400J	6.3 ± 0.9	8.1 ± 0.5	45	44	24.0	24.5	Pele
28dec1400K	2.6 ± 0.4	6.6 ± 0.4	56	43	27.2	28.1	Pillan
28dec1400L	1.7 ± 0.2	1.9 ± 0.3	48	56	61.0	62.0	Isum
28dec1400M	2.3 ± 0.3	4.9 ± 0.2	55	63	60.5	61.4	Marduk

Note: Uncertainties indicated in this table is derived from the aperture photometry measurement. An additional uncertainty linked to the error bar of the zero-point measurement estimated to 15% in Lp and 25% in Ms must be added on the value BEFORE viewing angle correction.

Table 5a: Result of the one-temperature fit and total output of identified hot spots.

Hot Spot Name	Date of Obs.	Temperature in K	Best Temp in K	Emission Area in km²	Total Output 10^{-12} W
Surt	18dec0730	440± 60	460	68 ± 2	0.17±0.01
Fuchi	20dec0730	313± 95	285	2222 ± 203	0.83±0.07
Dazhbog	18dec0730	338± 25	345	5166 ± 121	3.82±1.10
Loki	18dec0730	335± 20	325	11467 ± 324	7.27±0.20
Loki	28dec1400	348± 25	340	10284 ± 173	7.79±0.23
Sengen	18dec0730	538± 125	495	15 ± 1	0.05±0.01
Unnamed-F	28dec1215	590± 270	650	5 ± 1	0.05±0.01
Unnamed-F	28dec1400	473± 135	540	18 ± 1	0.08±0.01
Daedalus	28dec1215	390± 50	415	206 ± 11	0.35±0.01
Daedalus	28dec1400	328± 55	345	939 ± 53	0.75±0.05
Hephaestus	28dec1400	280± 90	325	531 ± 107	0.36±0.04
Ulgen	28dec1215	390± 110	430	163 ± 14	0.32±0.02
Ulgen	28dec1400	365± 130	350	841 ± 29	0.72±0.02
Pele	26dec1400	743± 225	700	10 ± 1	0.14±0.01
Pele	28dec0830	563± 45	540	59 ± 1	0.28±0.01
Pele	28dec1215	735± 80	760	9 ± 1	0.17±0.02
Pele	28dec1400	575± 180	505	73 ± 5	0.27±0.02
Pillan	26dec1400	378± 35	370	482 ± 9	0.51±0.01
Pillan	28dec0830	360± 30	375	586 ± 22	0.66±0.02
Pillan	28dec1215	368± 45	345	1231 ± 71	0.99±0.05
Pillan	28dec1400	370± 80	380	400 ± 11	0.47±0.02
Isum	26dec1100	430± 50	430	49 ± 1	0.09±0.01
Isum	26dec1400	408± 75	375	149 ± 10	0.17±0.01
Isum	28dec0830	380± 30	380	227 ± 1	0.27±0.01

Table 5b: Result of the one-temperature fit and total output of identified hot spots.

Hot Spot Name	Date of Obs.	Temperature in K	Best Temp in K	Emission Area in km^2	Total Output 10^{-12} W
Hot Spot	date of obs.	Temperature in K	best Temp in K	Emission area in km^2	Total Output 10^{-12} W
Marduk	26dec0700	408± 75	390	341 ± 9	0.45±0.01
Marduk	26dec1100	480± 70	475	73 ± 1	0.21±0.01
Marduk	26dec1400	508± 35	500	41 ± 1	0.14±0.01
Marduk	28dec0830	440± 20	430	178 ± 3	0.34±0.01
Marduk	28dec1215	513± 145	540	29 ± 1	0.14±0.01
Zamama	22dec1430	370± 160	370	136 ± 3	0.14±0.01
Zamama	26dec0700	460± 220	495	20 ± 1	0.07±0.01
Zamama	26dec1100	460± 180	435	48 ± 1	0.10±0.01
Zamama	26dec1400	695± 580	575	3 ± 1	0.02±0.01
Zamama	28dec0830	525± 310	680	3 ± 1	0.03±0.01
Prometheus	22dec1100	383± 115	325	1257 ± 175	0.81±0.10
Prometheus	22dec1430	393± 125	330	757 ± 111	0.51±0.07
Prometheus	26dec0700	423± 75	460	43 ± 3	0.11±0.01
Prometheus	26dec1100	383± 75	345	522 ± 47	0.42±0.04
Culann	22dec1430	308± 35	325	733 ± 38	0.46±0.03
Culann	26dec0700	453± 135	520	16 ± 2	0.06±0.07
Culann	26dec1100	385± 100	355	296 ± 16	0.27±0.02
Tupan	22dec1100	580± 240	610	4 ± 1	0.03±0.01
Tupan	22dec1430	415± 110	360	263 ± 29	0.25±0.03
Tupan	26dec0700	470± 120	485	18 ± 1	0.05±0.01
Thor	22dec1100	423± 25	420	352 ± 2	0.62±0.01
Thor	22dec1430	418± 25	430	252 ± 5	0.49±0.01
Thor	26dec0700	438± 75	475	105 ± 7	0.30±0.02
Amirani	22dec0730	323± 125	385	235 ± 45	0.29±0.05
Amirani	22dec1100	400± 110	390	210 ± 1	0.27±0.01
Amirani	22dec1430	368± 45	350	557 ± 22	0.47±0.02
Zal	20dec0930	405± 60	435	48 ± 3	0.10±0.01
Zal	22dec0730	355± 30	370	213 ± 9	0.23±0.01
Zal	22dec1100	350± 70	365	214 ± 10	0.22±0.01

Table 5c: Result of the one-temperature fit and total output of identified hot spots.

Hot Spot Name	Date of Obs.	Temperature in K	Best Temp in K	Emission Area in km^2	Total Output 10^{-12} W
Gish Bar	22dec0730	350± 40	370	723 ± 37	0.77±0.05
Gish Bar	22dec1100	353± 45	350	1264 ± 11	1.07±0.01
Gish Bar	22dec1430	338± 25	340	1362 ± 17	1.03±0.01
Unnamed-V	22dec0730	365± 40	360	849 ± 4	0.81±0.01
Unnamed-V	22dec1100	353± 25	360	969 ± 25	0.92±0.02
Unnamed-V	22dec1430	370± 30	355	976 ± 38	0.88±0.02
Tawhaki	20dec0930	395± 20	385	524 ± 11	0.65±0.01
Tawhaki	22dec0730	353± 35	370	963 ± 44	1.02±0.05
Tawhaki	22dec1100	380± 10	380	819 ± 1	0.97±0.01
Tawhaki	22dec1430	390± 50	370	884 ± 40	0.94±0.04
Janus	20dec0730	468± 75	505	44 ± 2	0.17±0.01
Janus	20dec0930	618± 115	615	14 ± 1	0.13±0.01
Janus	22dec0730	585± 120	595	24 ± 1	0.17±0.01
Masubi	20dec0930	398± 35	415	233 ± 8	0.39±0.02
Masubi	22dec0730	430± 50	440	176 ± 3	0.37±0.01
Uta	18dec0730	410± 90	440	59 ± 4	0.13±0.01
Uta	20dec0930	395± 90	415	83 ± 4	0.14±0.01

Table 6: Result of the basaltic lava cooling flow model applied on Pele and Isum brightness in Kc, Lp, and Ms in 28dec0830 data set images. The brightness labeled 1 and 2 correspond to two minimal and maximal intensities for each measurement taking into account the uncertainties introduced by the aperture photometry measurement

	Pele 2	Pele 1	Isum 1	Isum 2
K-brightness GW/sr/μm	2.8	4	2.4	3.2
L-brightness	7.6	8.4	1.4	1.6
M-brightness	10.3	10.5	3.5	3.7
Total area, km^2	50.94	21.95	1.45	0.9552
Total flux, GW	256.5	214.4	46.4	49.6
Low temp, K	473	562	771	879
Age of oldest surface, hrs	37.2	8	0.415	0.111
Implied dA/dt, m2/s	381.434	762.000	968.186	2380.8

Table 1: Power Outputs of 9 active centers detected by Galileo/PPR in I31 & I32 and during this observing run. Last column indicates the ratio between our measurements and I31.

name	I31	I 32	Keck AO	ratio
hot spot		10^{12}		I31
Dazhbog	3.59	4.38	3.82	1.1
Loki	15.2		7.6	2.0
Daedalus	1.79	1.43	0.55	3.2
Hephaestus	0.40		0.36	1.1
Ulgen	0.51	0.88	0.52	1.0
Pele	0.26	0.31	0.21/0.59	0.8/2.3
Pillan	2.35	1.51	0.66	3.8
Isum	0.44		0.18/0.12	2.4/3.6